A SLUGGS and Gemini/GMOS combined study of the elliptical galaxy M60: wide-field photometry and kinematics of the globular cluster system

Vincenzo Pota[1], Jean P. Brodie[1], Terry Bridges[2], Jay Strader[3], Aaron J. Romanowsky[1,4],
Alexa Villaume[1], Zach Jennings[1], Favio R. Faifer[5,6], Nicola Pastorello[7], Duncan A. Forbes[7]
Ainsley Campbell[2], Christopher Usher[7], Caroline Foster[8], Lee R. Spitler[8,9], Nelson Caldwell[10]
Juan C. Forte[5], Mark A. Norris[11], Stephen E. Zepf[3], Michael A. Beasley[12,13], Karl Gebhardt[14]
David A. Hanes[2], Ray M. Sharples[15], Jacob A. Arnold[1]

[1] *University of California Observatories, 1156 High Street, Santa Cruz, CA 95064, USA*
[2] *Department of Physics, Engineering Physics, and Astronomy, Queen's University, Kingston, ON K7L 3N6, Canada*
[3] *Department of Physics and Astronomy, Michigan State University, East Lansing, Michigan 48824, USA*
[4] *Department of Physics and Astronomy, San José State University, One Washington Square, San Jose, CA 95192, USA*
[5] *Consejo Nacional de Investigaciones Cientficas y Técnicas (CONICET)-Planetario Galileo Galilei, CABA, Rep. Argentina*
[6] *Instituto de Astrofísica de La Plata (CCT La Plata - CONICET - UNLP)*
[7] *Centre for Astrophysics & Supercomputing, Swinburne University, Hawthorn VIC 3122, Australia*
[8] *Australian Astronomical Observatory, PO Box 915, North Ryde, NSW 1670, Australia*
[9] *Department of Physics & Astronomy, Macquarie University, Sydney, NSW 2109, Australia*
[10] *Harvard-Smithsonian Center for Astrophysics, Cambridge, MA, USA*
[11] *Max Planck Institut für Astronomie, Königstuhl 17, D-69117 Heidelberg, Germany*
[12] *University of La Laguna. Avda. Astrofísico Fco. Sánchez, s/n. E38206, La Laguna, Tenerife, Canary Islands, Spain.*
[13] *Instituto de Astrofísica de Canarias. Calle Vía Láctea s/n. E38200 - La Laguna, Tenerife, Canary Islands, Spain.*
[14] *Astronomy Department, University of Texas, Austin, TX 78712, USA*
[15] *Department of Physics, University of Durham, South Road, Durham DH1 3LE*

March 2015

ABSTRACT

We present new wide-field photometry and spectroscopy of the globular clusters (GCs) around NGC 4649 (M60), the third brightest galaxy in the Virgo cluster. Imaging of NGC 4649 was assembled from a recently-obtained *HST*/ACS mosaic, and new Subaru/Suprime-Cam and archival CFHT/MegaCam data. About 1200 sources were followed up spectroscopically using combined observations from three multi-object spectrographs: Keck/DEIMOS, Gemini/GMOS and MMT/Hectospec. We confirm 431 unique GCs belonging to NGC 4649, a factor of 3.5 larger than previous datasets and with a factor of 3 improvement in velocity precision. We confirm significant GC colour bimodality and find that the red GCs are more centrally concentrated, while the blue GCs are more spatially extended. We infer negative GC colour gradients in the innermost 20 kpc and flat gradients out to large radii. Rotation is detected along the galaxy major axis for all tracers: blue GCs, red GCs, galaxy stars and planetary nebulae. We compare the observed properties of NGC 4649 with galaxy formation models. We find that formation via a major merger between two gas-poor galaxies, followed by satellite accretion, can consistently reproduce the observations of NGC 4649 at different radii. We find no strong evidence to support an interaction between NGC 4649 and the neighbouring spiral galaxy NGC 4647. We identify interesting GC kinematic features in our data, such as counter-rotating subgroups and bumpy kinematic profiles, which encode more clues about the formation history of NGC 4649.

1 INTRODUCTION

Galaxies are the building blocks of the visible Universe and the best tools to study its structure. Galaxies are alike in many ways, suggesting that similar underlying mechanisms regulate their for-

mation, but they are not identical to each other, implying that formation processes vary slightly from galaxy to galaxy (Lintott et al. 2008). While high redshift galaxy surveys can be used to infer "average" formation mechanisms for a sample of galaxies, studying nearby galaxies in detail can allow us to reconstruct their particular

and unique formation histories. Moreover, observations of galaxies at $z = 0$ provide the end product that computer simulations attempt to reproduce (e.g., Hoffman et al. 2010; Wu et al. 2014; Naab et al. 2014).

In the standard galaxy formation theory, small structures collapse first (White & Rees 1978; Searle & Zinn 1978; Zolotov et al. 2009), and then grow hierarchically into larger structures via galaxy mergers and/or via accretion of satellite galaxies (e.g., López-Sanjuan et al. 2010; Font et al. 2011; van Dokkum et al. 2014; Tasca et al. 2014). The latter is responsible for the building-up of galaxy outskirts (which we will refer to as stellar haloes) from high ($z \approx 2$) to low redshift (Tal & van Dokkum 2011; Oser et al. 2010; Khochfar et al. 2011). The various processes which shaped galaxies with time can be simulated and compared with observations of galaxies at a particular redshift. For example, minor mergers can create stellar shells and tidal streams observable in deep imaging (Tal et al. 2009; Ebrova 2013; Atkinson et al. 2013; Duc et al. 2015), whereas the secular accretion of satellite galaxies can be studied with photometry of stacked galaxies (e.g., Oser et al. 2010; Tal & van Dokkum 2011; D'Souza et al. 2014) or by studying the chemistry and kinematics of stellar haloes (e.g., Forbes et al. 2011; Romanowsky et al. 2012; Coccato et al. 2013).

Galaxy haloes are difficult to study because they are optically faint. Globular clusters (GCs), on the other hand, are much more observationally convenient for studying galaxy haloes. They are relatively easy to detect because of their high surface brightness and they generally populate haloes in large numbers (e.g., Brodie & Strader 2006). The outermost GCs can be used to map out halo properties (e.g., kinematics and metallicity) out to tens of effective radii (e.g., Ostrov et al. 1993; Schuberth et al. 2010a; Usher et al. 2012; Pota et al. 2013; Forbes et al. 2011). Their old ages and their direct connection with the star forming episodes in a galaxy's history (Strader et al. 2005; Puzia et al. 2005) mean that they are ideal tracers of the assembly processes that shaped the host galaxy (e.g., Romanowsky et al. 2012; Leaman et al. 2013; Foster et al. 2014; Veljanoski et al. 2014).

In this paper we study the GC system of the E2 early-type galaxy NGC 4649 (M60), the third brightest galaxy in the Virgo cluster. NGC 4649 is itself at the centre of a small group of galaxies and is the dominant member of the galaxy-pair Arp 116 (Arp 1966). The proximity to the disturbed spiral galaxy NGC 4647 (13 kpc in projection) potentially makes NGC 4649 an example of a pre major-merger between two massive galaxies in the local Universe, although this connection is still debated (Young et al. 2006; de Grijs & Robertson 2006).

Galaxies like NGC 4649 are ideal laboratories to test galaxy formation models. This galaxy has been scrutinized from different angles, revealing the portrait of a prototypical red and dead elliptical galaxy with a central supermassive black hole (Shen & Gebhardt 2010), dark matter halo (Bridges et al. 2006; Das et al. 2011) and X-ray halo (O'Sullivan et al. 2003; Das et al. 2010; Humphrey et al. 2008; Paggi et al. 2014).

Recent space-based observations of NGC 4649 (Strader et al. 2012; Luo et al. 2013; Norris et al. 2014), suggest that this galaxy interacted with a smaller galaxy with mass $M \sim 10^{10} M_\odot$ (Seth et al. 2014). This event should have deposited 100 GCs and many more stars into the halo of NGC 4649 during the course of its orbit (Harris et al. 2013). Indeed, asymmetries have been found in the two-dimensional distributions of GCs and low-mass X-ray binaries around this galaxy (Mineo et al. 2014; D'Abrusco et al. 2014), but these have not yet been linked to any particular interaction that occurred in NGC 4649.

In addition to recent space-based observations, the GC system of NGC 4649 has been studied with ground-based telescopes (Bridges et al. 2006; Pierce et al. 2006; Lee et al. 2008; Faifer et al. 2011; Chies-Santos et al. 2011). A spectroscopic follow up of 121 GCs (Hwang et al. 2008) revealed that the GC system of NGC 4649 has a large rotation amplitude. This is a rare feature in large early-type galaxies, whose GC systems are generally pressure supported with negligible or weak rotation (e.g., Côté et al. 2003; Bergond et al. 2006; Schuberth et al. 2010b; Strader et al. 2011; Norris et al. 2012; Pota et al. 2013; Richtler et al. 2014), although exceptions exist (e.g., Puzia et al. 2004; Arnold et al. 2011; Schuberth et al. 2012; Blom et al. 2012). On the other hand, Bridges et al. (2006) obtained radial velocities for 38 GCs in NGC 4649 and found no rotation, probably because of their relatively small sample size.
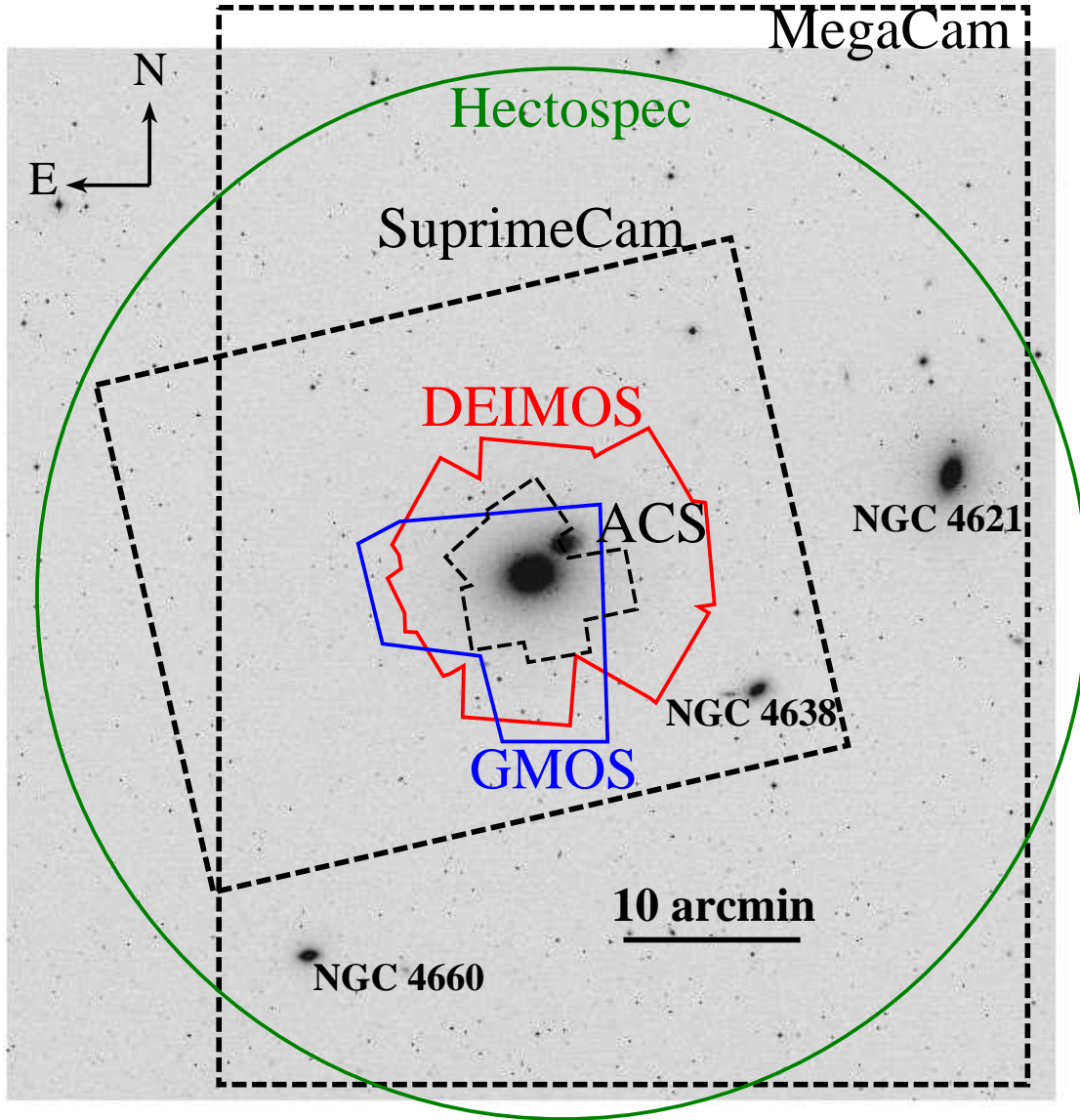
In this paper we present the largest spectro-photometric catalogue of GCs around NGC 4649. We construct a wide-field photometric GC catalogue by combining literature (*HST*), archival (CFHT) and new (Subaru) observations. We follow-up with spectroscopy of hundreds of GC candidates using joint observations from three multi-object spectrographs mounted on the Keck, MMT and Gemini telescopes. Our new spectroscopic catalogue is a factor of 3.5 larger than the current literature dataset (Lee et al. 2008) and has a factor of 3 greater velocity accuracy. This study exploits datasets from two complementary surveys of extragalactic GCs: the SLUGGS survey (Brodie et al. 2014), and an ongoing survey carried out with Gemini/GMOS (Bridges et al., in preparation). These two surveys combined, contribute 90 per cent of the final sample of confirmed GCs. We use the photometric and kinematic properties of the NGC 4649 GC system (including the blue and red GC subpopulations) to study the formation history of NGC 4649. A follow-up paper (Gebhardt et al., in preparation) will make use of the dataset presented in this work to model the mass content of NGC 4649.

We adopt a distance of 16.5 Mpc (Mei et al. 2007), an effective radius $R_e = 66$ arcsec $= 5.3$ kpc, an axis ratio $q = 0.84$ and a position angle $PA = 93$ deg (Brodie et al. 2014). Galactocentric distances R are expressed though the circularized radius $R = \sqrt{X^2 q + Y^2/q}$, where X and Y are the Cartesian coordinates of an object with NGC 4649 at the origin. The absolute magnitude of NGC 4649 is $M_B = -21.47$ mag or $M_V = -22.38$ mag.

This paper is structured as follows. Imaging observations and analysis are presented in Sections 2 and 3 respectively. The photometric results, including colour gradients and GC surface density are presented in Section 4. The spectroscopic observations and their outcomes are discussed in Section 5 and Section 6, respectively. We next explain the steps needed to build up the spectroscopic GC master catalogue: repeated GC measurements (Section 7) and colour and velocity uncertainty calibration (Section 8). We give an overview of the spectroscopic sample in Section 9 and explain the tools to quantify GC kinematics in Section 10. The kinematic modelling results are given in Section 11. We discuss our results in Section 12 and summarize the paper in Section 13.

2   IMAGING OBSERVATIONS

Imaging is the first step in identifying extragalactic GCs. It allows us to identify and characterize the photometric properties of the NGC 4649 GC system, and also to prune out the bulk of the con-

Figure 1. Overview of the observations. Shown is a Digitized Sky Survey image of NGC 4649 and surroundings. The field of view is 1 deg^2, which corresponds to 290 kpc $\times$ 290 kpc at this distance. NGC 4649 is the elliptical galaxy at the centre of the image, with the spiral NGC 4647 visible on the immediate right. Other galaxies in the field are labelled. Black dashed polygons represent the fields-of-view of the imaging cameras (labelled accordingly). Coloured solid outlines enclose the regions in the sky mapped by our three multi-object spectrographs (labelled). A 10 arcmin$\sim$ 48 kpc scale-bar is shown at the bottom of the image. North is up, East is left.

taminants (Galactic stars and background galaxies). Imaging is also necessary for selecting objects to be followed up spectroscopically.

Our imaging comes from three sources: *HST*/ACS, CFHT/MegaCam and Subaru/Suprime-Cam. The fields of view of the three instruments, along with the footprints of the multi-object spectrographs, are shown in Figure 1. CFHT/MegaCam covers the field of interest, and it was supplemented with Subaru/Suprime-Cam data to gain extra coverage on the East of NGC 4649 and to test for systematics in our ground-based photometry.

2.1 *HST*/ACS

The *HST* imaging is discussed in Strader et al. (2012) and we refer the reader to this paper for a detailed description of the data. The

dataset consists of six ACS pointings, which extend up to 6 arcmin from the galaxy center. The layout of the pointings is such that it avoids the foreground spiral NGC 4647. GC selection is based on $(g - z)$ colours, z magnitudes and half-light radii r_h. The latter can be measured down to $\sim 0.1\times$ FWHM (Spitler et al. 2006), which corresponds to ~ 0.7 pc at the distance of NGC 4649. Unresolved sources were not selected as GCs. The latter is the physical radius which contains half of the total light of the object. The final HST/*ACS* catalogue consists of 1603 GC candidates.

2.2 CFHT/MegaCam

The area surrounding NGC 4649 has been imaged with CFHT/MegaCam as part of the Next Generation Virgo Survey

(Ferrarese et al. 2012). MegaCam has a field-of-view of 0.96×0.94 deg^2 and a pixel scale of 0.187 arcsec/pixel. Reduced CFHT/MegaCam images and the respective weight-images in gri filters were downloaded from the CFHT/MEGAPIPE legacy archive (Gwyn 2008). Images are provided already calibrated to standard SDSS filters. The logs of the CFHT observations are given in Table 1. The seeing for all images is < 0.8 arcsec.

We use a total of five MegaCam pointings. Four of these are in $ugiz$-filters, but they are not centered on NGC 4649. A fifth pointing in the r-filter is centered on NGC 4649. The final CFHT field of interest spans roughly 1 degree in declination and half a degree in right ascension, as shown in Figure 1. We discard 30 arcmin in right ascension as we are not interested in the sky to the West of NGC 4621.

2.3 Subaru/Suprime-Cam

NGC 4649 was imaged with Subaru/Suprime-Cam in gri filters. The field-of-view of Suprime-Cam is 34×27 arcmin^2, with a pixel scale of 0.2 arcsec/pixel (Miyazaki et al. 2002). The camera was pointed at roughly the centre of NGC 4649. A summary of the Subaru observations is given in Table 1. The seeing was sub-arcsec for the g and i images, and 1.1 arcsec for the r image.

We use a custom made pipeline for reducing the Subaru Suprime-Cam imaging, based on the SFRED2 pipeline of Ouchi et al. (2004). The reduction consists of the following steps:

- We subtract the bias measured from the overscan regions for each chip. We create the flat field frames by median combining the dome-flats for each chip. We use L.A. Cosmic (vanDokkum 2001) to remove the cosmic rays from the object frames.
- We correct for chip-to-chip quantum efficiency variations and scale individual chips for any time-variable gain. We correct for the atmospheric distortion, mask out the auto-guider probe in each frame and sky subtract using a simple median of medians.
- We use a Monte Carlo sampling method to efficiently find the astrometric solution which minimizes the positional offsets between SDSS and point sources in our data.
- We multiplicatively scale each exposure to the median throughput level of all the exposures before co-adding them into a final image. The final mosaic image for each filter was performed with the software Montage [1].

3 IMAGING ANALYSIS

3.1 Catalogue extraction and calibration

We use SExtractor (Bertin & Arnouts 1996) to extract sources from the Suprime-Cam and MegaCam images. We extract sources from the two cameras separately, and we combine them later on. We run SExtractor on all the fields listed in Table 1. Only sources above 2.5σ are extracted. The zero point magnitude is set to 30 mag for the CFHT images (Ferrarese et al. 2012), and to 25 mag for the Subaru images. The weight-maps downloaded from the MegaPipe archive were used to optimise the extraction of MegaCam objects. The weight-map for the Suprime-Cam dataset was set to "background", meaning that we let SExtractor compute the variance map from the science images themselves.

For each extracted source, we measure: *a*) coordinates;

[1] http://montage.ipac.caltech.edu/index.html

Obs ID-Filter	Date	Exposure time	Seeing
	[HST]	[seconds]	[arcsec]
Subaru–g	2010-04-11	1160	0.8
Subaru–r	2010-04-11	1260	1.1
Subaru–i	2010-04-11	490	0.7
G008.190.711+11.596–r	2008-03-01	2160	0.8
NGVS+3+0–g	2009-02-27	3170	0.6
NGVS+3+0–i	2009-02-27	2055	0.6
NGVS+3-1–g	2009-02-27	3170	0.6
NGVS+3-1–i	2009-02-27	2055	0.6
NGVS+2+0–g	2009-02-25	3170	0.6
NGVS+2+0–i	2009-02-15	2055	0.6
NGVS+2-1–g	2009-05-25	3170	0.6
NGVS+2-1–i	2009-06-20	2055	0.6

Table 1. Ground-based photometric observations. Listed are the telescope and filter, the observation date in Hawaiian Standard Time (HST), the exposure time and the seeing. The overall seeing conditions are excellent.

b) `magbest`, which we use as our primary magnitude measurement; *c*) a set of magnitudes computed within different apertures (from 4 to 11 pixels in diameter); *d*) structural parameters, such as the ellipticity, position angle and FWHM.

The photometric properties of the objects in common between the different g and i MegaCam pointings are in good agreement with each other. Selecting objects brighter than $i = 23$ mag, we find the median magnitude difference to be $\Delta g = 0.006$ mag and $\Delta i = 0.008$ mag, respectively. The extracted properties for these objects are averaged together so that every object is unique, with magnitude measurements in all three filters.

Point sources are selected based on the difference between the magnitude measured within 4 pix and within 8 pix. This difference is small for point sources (typically < 0.6 mag) because their light profiles fall off more rapidly than those of extended sources. The latter become important source of contamination for $(i > 22$ mag$)$.

With the point-source catalogues in hand, we calibrate the magnitudes to standard SDSS gri filters. We select a bright subsample $(18 < i < 21$ mag$)$ and match these sources to the SDSS DR7 point-source catalogue, which covers the entire field-of-view in Figure 1.
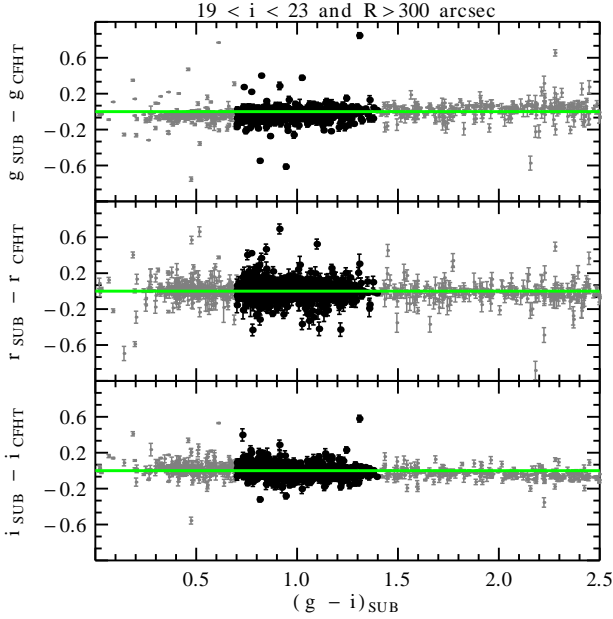
The MegaCam dataset was already calibrated to SDSS magnitudes and, in fact, we find the zero-point corrections to be always < 0.05 mag, within the photometric uncertainties. For the Suprime-Cam dataset we find: $g_{\mathrm{SDSS}} - g_{\mathrm{SUB}} = 3.46 \pm 0.05$ mag, $r_{\mathrm{SDSS}} - r_{\mathrm{SUB}} = 3.76 \pm 0.05$ mag, $i_{\mathrm{SDSS}} - i_{\mathrm{SUB}} = 3.66 \pm 0.04$ mag, respectively.

3.2 Comparison between CFHT and Subaru

Before merging the MegaCam and Suprime-Cam datasets, we study how the magnitudes extracted from both cameras compare with each other. We match the two catalogues selecting only bright $(19 < i < 23)$ objects outside $R = 300$ arcsec, because ground-based imaging is notoriously incomplete near the centres of the galaxies.

Figure 2 shows the magnitude difference in three bands of the ~ 1800 point sources in common between MegaCam and Suprime-Cam. We are mostly interested in objects with $0.65 \leqslant (g-i) \leqslant 1.4$ because this is the colour range populated by extragalactic GCs, as we will discuss below. In this specific colour-magnitude range, the

Figure 2. Comparison between Subaru and CFHT datasets. Top, central and bottom panel shows the magnitude difference in g, r, i filters, respectively, of the point-sources in common between Subaru and CFHT. The green line marks zero magnitude difference. Only objects with $19 < i < 23$ and $0 < (g - i) < 2.5$ are shown. Globular clusters fall in the colour range $0.07 \leqslant (g - i) \leqslant 1.4$, which is highlighted with black points. In this colour range, the CFHT and Subaru datasets agree with each other. The deviation of ~ 0.07 mag for g and i filters, and ~ 0.09 mag for the r band.
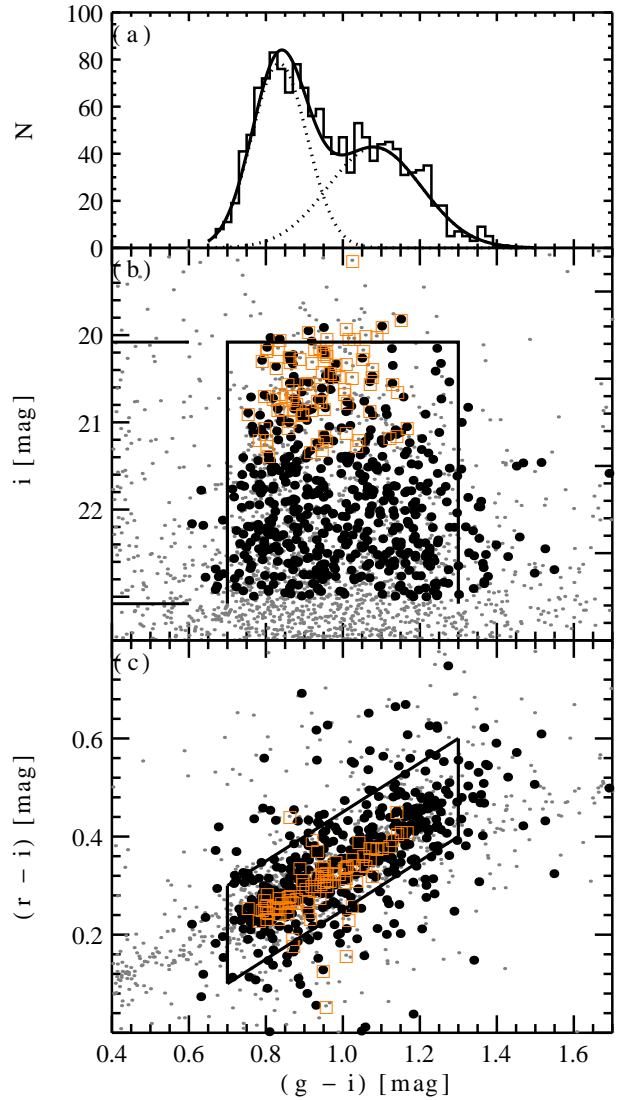
root-mean-square (rms) of the magnitude difference is $\mathrm{rms}(\Delta g) = 0.070$ mag, $\mathrm{rms}(\Delta r) = 0.095$ mag, $\mathrm{rms}(\Delta i) = 0.064$ mag for the g, r, i filters respectively. The larger value of $\mathrm{rms}(\Delta r)$ is due to the relatively poor quality of the Suprime-Cam r-band image. No significant trend with $(g - i)$ colours is observed in the colour range under investigation. We conclude that the magnitudes measured from MegaCam and from Suprime-Cam are in good agreement.

We then combine the point-source catalogues from Mega-Cam and Suprime-Cam. If an object is present in both datasets, we weight-average its magnitudes in the three filters. If an object is present in only one catalogue, it is added to the final master catalogue without applying any magnitude correction. Lastly, we correct the final gri magnitudes for Galactic extinction using $A_g = 0.087$ mag, $A_r = 0.060$ mag, $A_i = 0.045$ mag, respectively (Schlafly & Finkbeiner 2011).These values vary by 10 per cent across our field-of-view of interest. The combined MegaCam–Suprime-Cam point-source catalogue consists of ~ 20500 unique objects, including interlopers.

3.3 Globular cluster selection

We use two steps to extract bona-fide GCs from the point-source catalogue. We first exploit the *HST*/ACS catalogue to check where GCs lie in colour-colour and colour-magnitude space, and then we select GCs based on this comparison.

GCs are partially resolved in *HST* images. In NGC 4649 the average GC half-light radii are $r_h \approx 2$ pc (Strader et al. 2012), similar to what is found in other galaxies (e.g., Masters et al. 2010). This means that even without spectroscopic confirmation, we can

Figure 3. Colour-magnitude and colour-colour magnitude diagrams. For clarity, only ground-based sources within 600 arcsec from NGC 4649 are shown (small grey points). Large black points are partially resolved GCs from HST. Orange open squares are the confirmed GCs from Hwang et al. (2008). The bottom panel shows the colour-colour magnitude plot. The central panel is the colour-magnitude plot. Horizontal lines indicate the TOM of the GC luminosity function $i\,(\mathrm{TOM}) = 23.1$ mag, and the magnitude of ω Cen, $i = 20$ mag. Objects inside the black lines are flagged as GC candidates. The top panel is the numerical histogram of the selected GCs, with the best double-Gaussian fit to the data.

flag objects with apparent $r_h < 10$ pc as GCs likely associated with NGC 4649, although some contamination is expected at faint magnitudes. From the ACS catalogue, we select GC candidates brighter than $z = 23$ mag and with $R > 100$ arcsec and we match them with our combined ground-based catalogue.

We find roughly 500 objects in common. Then we look at the colour-magnitude and colour-colour diagrams of the point sources with ground-based photometry, and we highlight these 500 GCs with size confirmation. The result is shown in Figure 3. We also matched the ACS catalogue with the 121 spectroscopically confirmed GCs from Hwang et al. (2008), which will be discussed in

Section 5. We found 84 objects in common, which are also shown in Figure 3.

NGC 4649 GCs populate a well defined area of both the colour-magnitude and colour-colour diagrams. In the central panel of Figure 3 we see the well known GC colour bimodality and the blue tilt, which causes the most luminous blue GCs to bend towards redder colors (e.g., Spitler et al. 2006; Harris et al. 2006). At the faint and bright GC selection limits we show, respectively, the expected turn-over magnitude (TOM) of the GC luminosity function ($M_{\rm TOM}, i = -7.97$ mag; Jordán et al. 2007) and the magnitude of ω Cen, the brightest star cluster in the Milky Way, for which we assume a magnitude $M_i = -11.0$ mag ($i = 20.1$ mag) obtained from Vanderbeke et al. (2014) adopting the distance of van de Ven et al. (2006). A handful objects are indeed brighter than this magnitude. We will show that some of these are ultra compact dwarfs (UCDs) with spectroscopic confirmation (see §9).

On the bottom panel of Figure 3 we notice the same grouping of GCs in a narrow colour-colour range. The tail of objects at very red colours are Galactic red giant stars which enter the GC main sequence at $(g-i) \sim 1.4$ mag and contaminate the sample. The objects at $(g-i) \leqslant 0.6$ are Galactic blue young stars. Roughly 20 per cent of the GC candidates lie outside the selection box. This is due to photometric uncertainties and to the poor quality of ground-based photometry near the centre. Selecting only objects with $z < 22$ mag and with $R > 200$ arcsec, the fraction of outliers reduces to 3% .
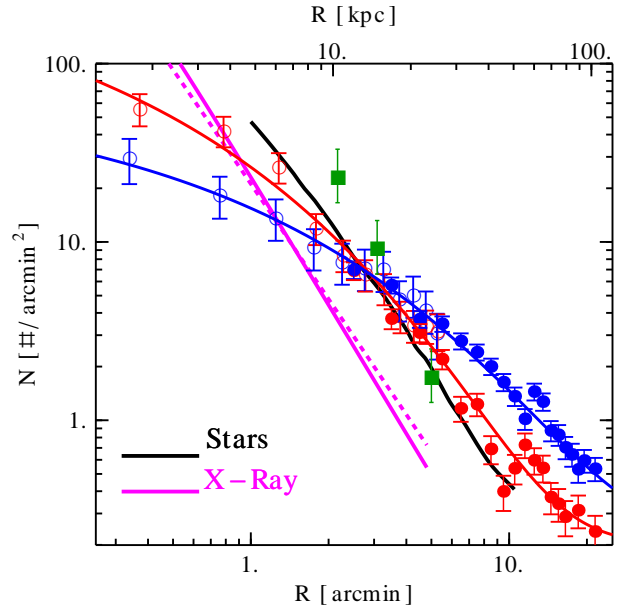
Objects falling in the colour range highlighted in Figure 3 are flagged as GC candidates. Objects falling outside the selection box by less than 1σ are also flagged as GCs. We require a GC to be brighter than the turn-over-magnitude ($i < 23.1$ mag) and fainter than ω Cen. These selection criteria returned ~ 4000 GC candidates, with a 14 per cent contamination rate based on the background value which will be computed in Section 4.

The colour distribution of the selected GCs is bimodal (top panel of Figure 3). To quantify this bimodality, we use the Kaye's Mixture Model (KMM) algorithm (Ashman et al. 1994) to fit a double-Gaussian to the GC colour distribution. This calculation was performed only on objects within 600 arcsec from the galaxy centre in order to prune the bulk of contaminants which populate the outer regions of the galaxy (see Section 4).

We find bimodality to be statistically significant with a p-value $< 10^{-4}$. The blue GC subpopulation is fitted by a Gaussian which peaks at $\mu(g-i) = 0.83$ mag, with a dispersion of $\sigma(g-i) = 0.07$ mag. For the red GC subpopulation, we find $\mu(g-i) = 1.08$ mag, with a dispersion of $\sigma(g-i) = 0.12$ mag. For comparison, Faifer et al. (2011) found the following values based on Gemini/GMOS photometry: $\mu(g-i) = 0.78$, $\sigma(g-i) = 0.09$, and $\mu(g-i) = 1.08$, $\sigma(g-i) = 0.11$, for the blue and red subpopulations, respectively. The local minimum of the combined double-Gaussian is at $(g-i) = 1.0$ mag. This is the value adopted to separate blue and red GCs in our ground-based imaging.

4   PHOTOMETRIC RESULTS

We now use our photometrically-selected GCs to study two important relations: how the GC number density and the GC colours vary with radius. The first is an essential observable for dynamical modelling of galaxies, but it is also needed to quantify contamination from interlopers. The shape of the second relation is an important prediction of theories of the hierarchical growth of galaxies.

Figure 4. Globular cluster surface density profiles. Blue and red GCs are colour-coded accordingly. Open and filled circles are from *HST*/ACS and from ground-based photometry, respectively. The two solid lines are the best fits to equation 1. Green squares are PNe data. The black line is the arbitrarily re-normalized stellar surface brightness profile of NGC 4649 in the V-band from Kormendy et al. (2009). The magenta thick and dashed lines are the outer slope of the X-ray surface brightness profile from *ROSAT* and from *Chandra*, respectively. The red GCs are more centrally concentrated than the blue GCs.

4.1   Globular cluster surface density

We divide our sample into blue and red GCs at $(g-i) = 1.0$ mag. We count the number of GCs in elliptical annuli centered on NGC 4649 and we divide this number by the area of the annulus. Saturated stars, surrounding galaxies and chip gaps in the CHFT images were masked out. For each bin, we compute the Poissonian error using $\sqrt{N}$/ Area, where N is the number of objects per bin.

As our ground-based imaging is incomplete near the galaxy centre, we supplement our data with the ACS GC surface density profile from Mineo et al. (2014) (their Figure 2), which covers the innermost 5 arcmin of the galaxy. This was obtained selecting GCs brighter than $z < 22.2$ mag and it was renormalized to match the galaxy surface brightness. Therefore, the ACS surface density profile does not represent absolute counts of objects with $z < 22.2$. We construct the ground based surface density profile selecting GCs about 1 magnitude fainter with respect to ACS. To account for this normalization difference, we count the GCs selected with our criteria in the radial range $150 < R < 270$ arcsec, and we compare it to the number of GCs from Mineo et al. (2014) (their Figure 2) in the same radial range. We find that a factor of 4.3 and 5.7 is needed to match the ACS-based surface density profile for the blue and red GCs respectively, with our ground-based surface density profiles.

The combined GC surface density profiles for the blue and red GCs are shown in Figure 4.

At first glance, our results show the typical spatial features seen in other GC systems: the red GCs are more centrally concentrated, while the blue GCs are more extended (e.g., Bassino et al. 2006). The flattening of the number density at large radii is due to contaminants (faint Galactic stars and unresolved galaxies), and

marks the detectable boundary of the GC system. To quantify the background level bg, assumed to be constant across the entire image, we fit the blue and red GC data with a modified Sérsic (1963):

$$N_{GC}(R) = N_e \times \exp\left(-b_n\left[\left(\frac{R}{R_e}\right)^{1/n} - 1\right]\right) + bg, \quad (1)$$

where n is the Sérsic index and N_e is the surface density at the effective radius R_e. The parameter b_n is linked to n via $b_n = 1.9992n - 0.3271$.

The best fits to equation 1 are shown in Figure 4. For the red GCs, we find $R_e = 4.1 \pm 1.1$ arcmin $= 20 \pm 7$ kpc, $n = 2.5 \pm 0.5$ and $bg = 0.2 \pm 0.1$ objects/arcmin^2. For the blue GCs, we find $R_e = 12.6 \pm 7.1$ arcmin $= 60 \pm 34$ kpc, $n = 2.4 \pm 0.6$ and $bg = 0.23 \pm 0.19$ objects/arcmin^2. Therefore the blue GC system is a factor of three more extended than the red GCs.

In Figure 4, we also compare the GC spatial distribution with the surface density of the following tracers: (i) the stellar surface brightness profile of NGC 4649 in the V-band from Kormendy et al. (2009); (ii) the X-ray surface brightness profile from *ROSAT* (O'Sullivan et al. 2003) and from *Chandra* (Paggi et al. 2014). In this case, we show a β-model best fit to X-ray data. The best fit is shown up to the radius where the X-ray emission drops below the background level (~ 4.8 arcmin) for the *ROSAT* data. (iii) Planetary nebulae (PNe) surface density data from Das et al. (2011), with the caveat that these were obtained selecting objects within a cone aligned with the galaxy major axis. The three tracers were arbitrarily re-normalized in order to be compared with the GC surface density profiles.
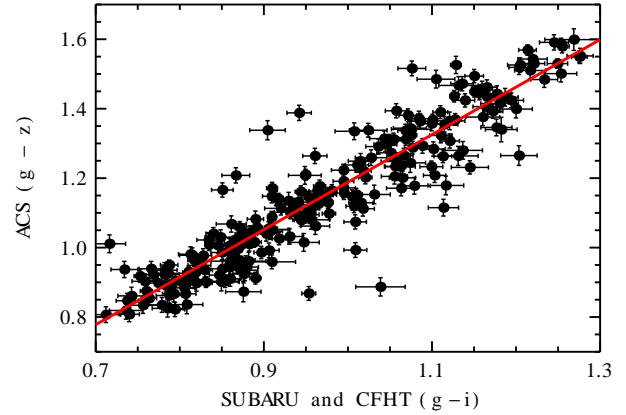
We can see that the slope of the stellar and X-ray surface brightness is qualitatively similar to the slope of the red GCs, with the caveat that this similarity is dependent on the arbitrary normalization. X-ray haloes are usually more extended than the stellar component (Sarazin et al. 2001; Forte et al. 2005; Forbes et al. 2012). Results from *Chandra* and from *ROSAT* are consistent with each other. The similarity between stars–PNe and red GCs is expected if the galaxy bulge and the red GCs formed in a similar fashion at similar epochs (e.g., Shapiro et al. 2010).

We follow the approach of Forbes et al. (2012) to quantify the similarities between the distribution of GCs and X-ray gas. We fit the GC density profiles in Figure 4 with a β-model, which is a cored-power law described by $I(r) \propto r^{-3\beta+0.5}$, where β is the power-law slope we are interested in. The background values bg derived above were taken into account during the fit. A fit to the *ROSAT* data returns $\beta_X = 0.56 \pm 0.08$ (O'Sullivan et al. 2003). Using new deep *Chandra* data from Paggi et al. (2014), one obtains consistent results with $\beta_X = 0.52 \pm 0.01$. For the red and blue GCs, we find $\beta_R = 0.48 \pm 0.03$ and $\beta_B = 0.44 \pm 0.05$, respectively. In this case the larger uncertainty reflects the uncertainty on the GC background value. This exercise shows the outer slope of blue and red GCs are consistent within the errors, but the red GC profile is slightly steeper and more similar to the X-ray slope.
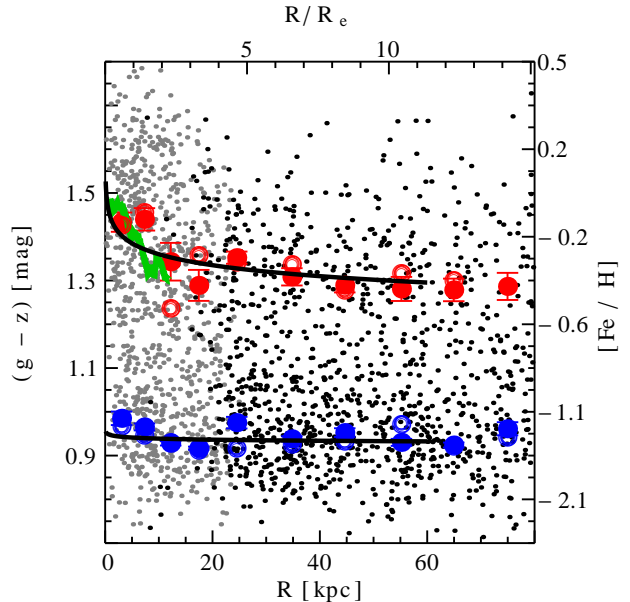
4.2 Globular cluster colour gradients

We study the radial variations of GC colours by combining *HST* and ground-based imaging. It is more efficient to calibrate both datasets to a common photometric colour and then merge them. We choose to transform the ground-based $(g - i)$ to ACS $(g - z)$ because this can be then be converted to metallicity through the conversion of Peng et al. (2006).

As in the previous section, we match the objects in common

Figure 5. Photometric calibration between ground-based and space-based observations. Data points represent partially resolved GCs in *HST* images, with constraints on galactocentric distance and magnitude (see text). The red line is a weighted least-squares fit to the data.

Figure 6. Radial variation of GC colours. Grey and black small points are GC candidates from *HST* observations and from our ground based imaging, respectively. Black lines are best fits to the data up to 60 kpc (see text). Blue and red filled large circles show the colour peaks from KMM for a given radial range. Blue and red open large circles represent the peaks of the Gaussian-smoothed colour histogram in each bin (see text). The green line is the stellar metallicity profile converted to $(g - z)$ (see text). The GC subpopulation colour gradients are steeper towards the galaxy centre.

between *HST* and the combined Subaru+CFHT catalogue. We require ACS sources to be partially resolved with sizes $r_h < 10$ pc and magnitudes $19 < i < 22$ mag. We only consider sources with galactocentric radius $100 < R < 400$ arcsec because the ground-based imaging is unreliable within 100 arcsec.

We find 241 objects obeying the above criteria. A weighted last-squares fit to the data returns the colour transformation we are interested in:

$$(g - z) = (-0.18 \pm 0.03) + (1.36 \pm 0.03)(g - i) \quad (2)$$

The best fit, along with the data, is shown in Figure 5. The rms of the data with respect to the best fit line is 0.08 mag. The quality of the fit is satisfactory. We also convert the ACS g magnitudes to ground based g magnitudes. We find $g_{ACS} = (0.62 \pm 0.20) + (0.97 \pm 0.01)g$ with an rms scatter of 0.09 mag. Similarly, we find $z_{ACS} = (0.07 \pm 0.25) + (0.99 \pm 0.01)i_{ACS}$, with a scatter of 0.13 mag. We apply eq. 2 to our ground-based GC catalogue and we merge this into the ACS catalogue. Repeated objects are counted once and priority is given to objects with ACS photometry.

We construct the colour gradients by selecting ($21 < z < 23$) (consistently with Strader et al. 2013) to avoid contamination from interlopers at faint magnitudes and from the blue-tilt at bright magnitudes. We also clip objects within 5 arcmin of large galaxies in the field to avoid mixing their GC systems with that of NGC 4649. The results are shown in Figure 6.

We can see that the ACS and ground-based datasets agree and that they are complementary to each other. We study the colour profiles out to ~ 16 arcmin ~ 80 kpc, as dictated by the background estimate from equation 1. This radius corresponds to 15 R_e, where $R_e = 66$ arcsec is the effective radius of the diffuse starlight.

We compute GC colour radial profiles using two different methods. First, we bin the data radially with a 5 kpc bin size for the innermost 20 kpc, and with a 10 kpc bin size for $R > 20$ kpc. For each bin, we fit a double Gaussian with KMM, and derive the blue and red colour peaks of the fitted Gaussians. Second, we smooth the colour distribution with a Gaussian kernel of 0.05 mag and we find the blue and red peaks of the resulting smooth distributions. This second method is model independent, whereas the first method requires assumptions that may not provide a realistic representation of the data. The results are shown in Figure 6 as filled points for the first method (KMM) and open points for the second method (smooth kernel), respectively. We also compare our results with the stellar metallicity profile from Pastorello et al. (2014), converted from $[Z/H]$ to $(g - z)$ using equation B1 from Usher et al. (2012).

We can see that the results in Figure 6 are not very sensitive to the method adopted to compute the colour peaks. Both the blue and the red GCs show negative gradients within ≈ 20 kpc, as already found in Strader et al. (2012). Outside this radius, the colour gradients are consistent with being constant. The overall slope of the stellar colour profile is in good agreement with the results for the red GCs. This provides further evidence that stars from the galaxy spheroid and red GCs were assembled in a similar fashion, at least in the very central regions.

We quantify the gradients by fitting the function $(g - z) = a \log(R/R_e) + b$, where $R_e = 5.3$ kpc is the stellar effective radius of NGC 4649. We fit all individual GC datapoints in Figure 6 up to 60 kpc to minimize contamination from background sources. We divide the two GC subpopulations by adopting a cut at $(g - z) > 1.2$ for the red GCs and $(g - z) < 1.1$ for the blue GCs, respectively. This is done to avoid mixing between the two GC subpopulations at intermediate colours. For the red GCs, we find $a = -0.07 \pm 0.01$ and $b = 1.44 \pm 0.01$. For the blue GCs, we find $a = -0.005 \pm 0.010$ and $b = 0.94 \pm 0.01$, indicating an overall shallower colour gradient with respect to the red GCs.

The red GC colour gradient is wiggly in the range between 10 and 20 kpc, suggesting the presence of substructures in the data (Strader et al. 2012; D'Abrusco et al. 2014), and it is very steep inside 10 kpc. This is due to a group of GCs with very red colours $(g - z) > 1.5$, which populate only the innermost 10 kpc of the galaxy.

5 SPECTROSCOPY

Our spectroscopic sample comes from three multi-object spectrographs: Keck/DEIMOS, MMT/Hectospec and Gemini/GMOS. The footprint of the observations of each instrument is shown in Figure 1. The spectral coverage of the three spectrographs is diverse, but some spectral regions overlap. Figure 7 shows one of the nine GC spectra observed by all three spectrographs. In this section we describe the acquisition and reduction of the spectroscopic data.

5.1 Keck/DEIMOS

DEIMOS is a multi-object spectrograph mounted on the 10 meter Keck II telescope (Faber et al. 2003). One DEIMOS mask covers 15×6 arcmin^2 on the sky and it can contain up to 150 slits.

A total of four DEIMOS masks were observed around NGC 4649. Three masks were observed on 2012 Jan 17, and the fourth mask was observed on 2013 Jan 11. Slitmasks were designed giving priority to ACS GC candidates with size measurements. If no space-based photometry was available, slits were assigned to bright sample of GCs selected from the CFHT imaging discussed in Section 3. Suprime-Cam images were not yet available at the time of the mask design.

All observations were performed in sub-arcsec seeing conditions. The exposure time was 2 hours per mask. The instrument setup consisted of a 1200 l/mm grating, a dispersion of 0.33 Å/pixel, a slit width of 1 arcsec and the OG550 filter. With this setup the GC spectra cover the region from the Hα line (6563 Å) to the Calcium Triplet (CaT) feature (8500-8700 Å), with a median velocity accuracy of ~ 15 km s^{-1}. The spectra were reduced with a dedicated pipeline, which returns calibrated, sky-subtracted one-dimensional spectra (Cooper et al. 2012; Newman et al. 2013).
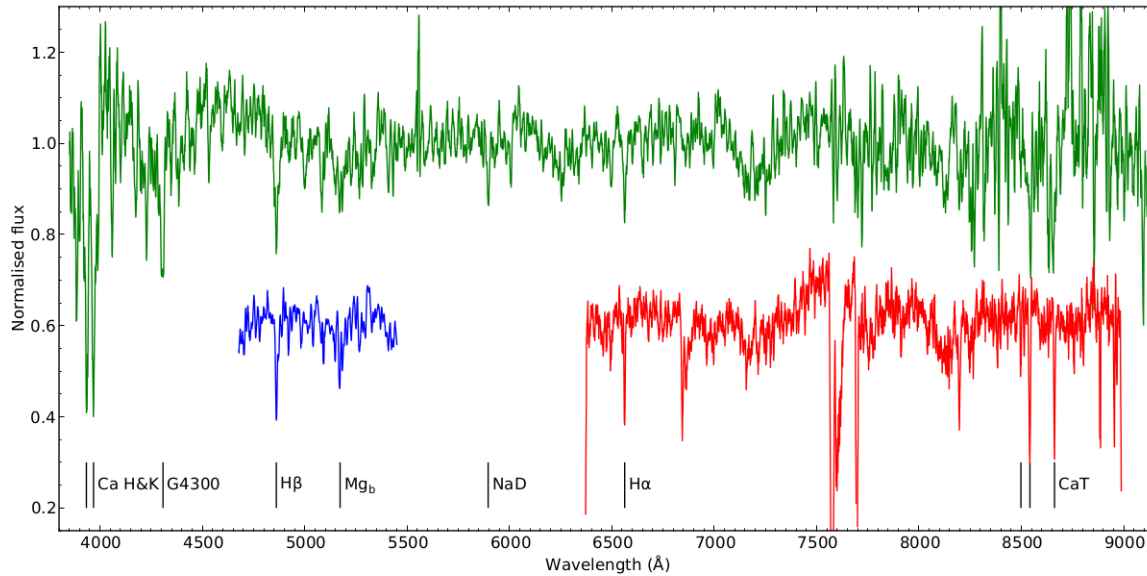
GC radial velocities were measured with iraf/fxcor using thirteen stars of different spectral type as templates observed using the same set-up. The average velocity scatter between different stellar templates is ~ 3 km s^{-1} for all four DEIMOS masks. The Doppler shift was computed solely from of the CaT lines, because the Hα line was not always covered with our instrument setup. The final GC radial velocity was taken as the average of the values from the thirteen stellar templates. The redshift-corrected spectra were inspected by eye to check that the CaT lines laid at the rest frame wavelength. The error budget on the velocity takes into account both the internal error given by fxcor and the scatter due to different stellar templates.

5.2 Gemini/GMOS

GMOS is a multi-object spectrograph and imager mounted on the 8-meter GEMINI telescopes (Hook et al. 2004). The GMOS camera has three 2048×2048 pixel CCDs with a scale of 0.07 arcsec/pixel and a field of view 5.5×5.5 arcmin^2. GMOS was used to obtain spectra for globular clusters in five fields in NGC 4649 (see Figure1). GC selection was performed as described in Faifer et al. (2011). GC spectroscopy for a field positioned near the galaxy center (Field 1) was obtained in May 2003 on Gemini North and was presented in Bridges et al. (2006) and Pierce et al. (2006), while spectroscopy for four additional fields (Fields 2-5) was obtained in the spring of 2010 on Gemini South and presented in this paper.

GC candidates for follow-up spectroscopy were selected using Sloan g' and i' images taken with GMOS-N in April 2002. Images were combined and median-filtered and run through iraf/daophot to

Figure 7. Spectrum of a globular cluster of NGC 4649 as seen from the three multi-object spectrographs used in this paper. Red is DEIMOS, blue is GMOS and green is Hectospec. Spectra are shifted to the rest frame wavelength. An arbitrary vertical offset is applied. Important absorption lines are labelled. Note that the Hectospec spectrum was corrected for telluric absorption, while the DEIMOS spectrum was not, which explains why the strong water absorption feature at ∼7700Å appears in the latter but not the former. The globular cluster's ID is D28. Its apparent magnitude is $z = 20.3$, and its radial velocity is $1160 \pm 7 \, \mathrm{km \, s^{-1}}$.

obtain photometry for point-like objects. The instrumental photometry was calibrated using F555W and F814W *HST*/WFPC2 photometry. A final sample of globular cluster candidates was obtained using magnitude ($9 < V < 22.5$ mag) and colour (0.75 mag $< V - I < 1.4$ mag) cuts. Extended sources were eliminated by eye, leaving 250 globular cluster candidates. A GMOS multi-slit mask was made for Field 1 using the standard Gemini GMMPS software, containing 39 object slits.

For the Fields 2-3-4-5 (program ID GN-2010A-Q-37), GMOS images in the SDSS $g'r'i'$ filters were taken in 2007A and 2009A to select GC candidates for multi-slit spectroscopy. Colour and magnitude cuts and image classification using SExtractor were used to obtain a final sample of GC candidates in each of the four fields. The GMMPS software was used to create multi-slit masks, and with the use of filters to restrict wavelength coverage, we were able to put slits on between 48 to 69 globular cluster candidates in the four fields. Some marginal objects were included to fill the mask, and we also placed some slits on the diffuse galaxy light.

Spectroscopy for Field 1 (program ID GN-2003A-Q-22) was obtained using GMOS-N in multi-slit mode in May and June 2003. A total of 8×1800 sec exposures were obtained with a central wavelength of 5000 Å, and 8×1800 sec were obtained with a central wavelength of 5050 Å, giving a total of 8 hours on-source time. We used the B600 grating, giving a dispersion of 0.45 Å/pixel, a resolution of ~ 5.5 Å, which corresponds to 320 km s^{-1} velocity resolution. Spectral coverage was typically from $3300-5900$ Å, and the seeing ranged from 0.65 to 0.9 ″over the four nights of observation. Bias frames, dome flat-fields and CuAr arcs were also taken for calibration.

Spectroscopy for the remaining four fields was obtained at GMOS-S in the spring of 2010. We obtained between 5 to 7.5 hours on-source per field, and conditions were good with seeing between 0.5 and 1.0 arcsec.

Data reduction was carried out using the Gemini/GMOS IRAF package, and consisted of the following steps: (i) a final spectro-

scopic flat-field was created; (ii) object frames were bias-subtracted and flat-fielded; (iii) the arc frame was reduced and used to establish the wavelength calibration; (iv) object frames were wavelength calibrated and sky-subtracted; (vi) 1D spectra were extracted from each object frame and median combined.

Iraf/fxcor was used to obtain radial velocities for each object via cross-correlation, using the MILES spectral library (Sánchez-Blázquez et al. 2006) as template. In this case, the template with the highest cross-correlation coefficient was used, although the relative scatter between templates was $\sim 4-5$ km s^{-1}, well within the measurement errors.

Before accounting for overlaps, there were ~ 185 objects with reliable velocities in fields 2-3-4-5. Astrometry and photometry for this sample were obtained from Faifer et al. (2011). Globular clusters from Field 1 (Bridges et al. 2006) were then added to this list, and objects observed in more than one field were identified.

5.3 MMT/Hectospec

Hectospec is a multi-fibre spectrograph mounted on the 6.5 meter MMT telescope (Fabricant et al. 2005). It has a 0.78 deg^2 field-of-view which can be filled with up to 300 fibers.

GC candidates were selected from the MegaCam and ACS images. Bright objects at large radii were favoured, although this naturally increases the contamination from Galactic stars. Due to the wide Hectospec field-of-view, GC systems in galaxies surrounding NGC 4649 (like NGC 4621 and NGC 4638) were also observed. Therefore, some contamination is expected from these galaxies.

One single Hectospec field was observed on May 16 and May 19, 2012, using a 270 l/mm grating, with a dispersion of 1.21 Åpixel, and a spectral resolution of ~ 5 Å, which corresponds to a velocity resolution of ~ 300 km s^{-1}.

Raw data were reduced as described in Mink et al. (2007). Heliocentric radial velocities were measured by cross-correlating the science spectra with a Hectospec template of an M31 GC. Er-

rors were estimated through Monte Carlo simulations with an additional 8 km s^{-1} to account for the wavelength calibration (see also Strader et al. 2011).

6   OUTCOME OF THE SPECTROSCOPIC FOLLOW-UP

We observed ~ 600 objects with DEIMOS, targeting ~ 500 photometrically selected GCs. We found 304 spectra (including duplicates between masks) consistent with the systemic velocity of NGC 4649. 23 additional GCs were discarded as "marginal" because the team could not reach a consensus on whether or not the features seen in their spectra were actual spectral lines. In addition, we found 13 Galactic stars and 56 background galaxies. The latter were identified via the strong emission lines in their spectra. However we do not measure the redshift of background galaxies. The remaining slits were unclassified, because the signal-to-noise was too low to retrieve any physical information from the spectrum. After accounting for repeated objects, the median velocity uncertainty of the DEIMOS GC sample is $\Delta v = 11$ km s^{-1}.

We observed a total of 187 objects with Gemini/GMOS, finding 172 extragalactic GCs, 14 Galactic stars and 1 background galaxy. The 172 GCs also include the 38 GCs observed by Pierce et al. (2006). GMOS maps the innermost 6 arcmin of NGC 4649 and it overlaps nicely with the DEIMOS field-of-view. The median velocity uncertainty of this sample is $\Delta v = 12$ km s^{-1}.

We observed 478 objects with Hectospec, and we found 102 extragalactic GCs (including duplicates), 157 background galaxies and 119 Galactic stars. The remaining fibres were unclassified. The median velocity uncertainty of this sample is $\Delta v = 14$ km s^{-1}, but in Section 7 we will explain that the effective uncertainty is larger than this value.
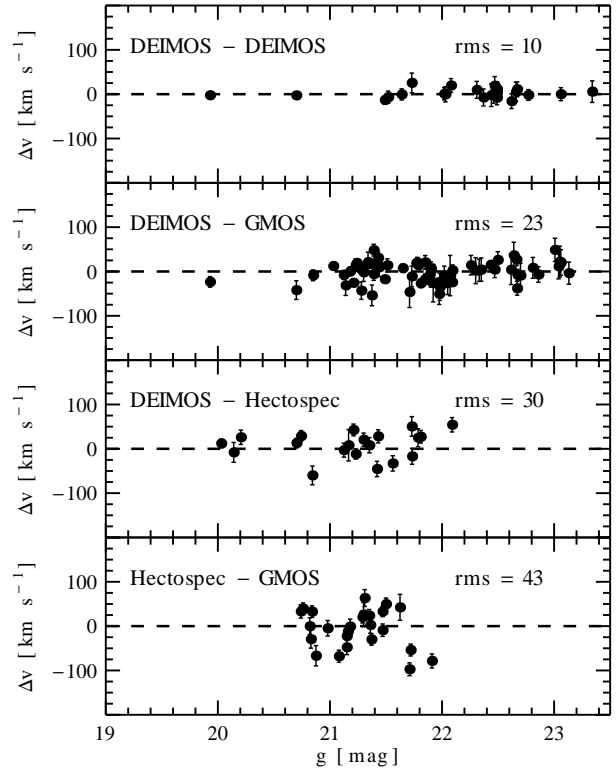
7   REPEATED MEASUREMENTS

We quantify how the radial velocity of a given GC compares to the radial velocity of the same GC observed over multiple spectrographs. We denote radial velocities from DEIMOS, GMOS and Hectospec wih v_D, v_G and v_H respectively. The uncertainties of the repeated objects are the sum in quadrature of the uncertainties of the single objects. The comparison between the three catalogues is illustrated in Figure 8 and discussed in the followings.

7.1   Duplicates from the same spectrograph

We find 26 and 33 GCs repeated across different DEIMOS and GMOS masks, respectively. For DEIMOS, the weighted-mean of the velocity difference of the objects in common is $\langle v_D - v_D \rangle = -0.6$ km s^{-1}, with an root-mean-square difference rms= 10 km s^{-1}. We conclude that the DEIMOS radial velocities are robust, and no additional velocity offset is needed.

For GMOS, we find field to field offsets in the range $|\langle v_G - v_G \rangle| = 25 - 40$ km s^{-1}, which probably reflects the different instrument set-ups of the five GMOS fields. The repeated radial velocity measurements from the five fields are generally consistent within 2σ. We decided to simply average the repeated GMOS GCs with no rigid offset, and use the comparison with the DEIMOS sample to renormalize the velocity uncertainties of the GMOS sample (see §7.3).

Figure 8. Repeated radial velocity measurements. Each panel shows the velocity difference for the objects in common between different catalogues (labelled on the top left) vs the magnitude in the g band. The top panel shows the comparison between GCs observed over different DEIMOS masks. The rms scatter in units of km s^{-1} of the velocity difference is reported on the top right of each panel. The velocity agreement is usually good (always < 100 km s^{-1}), although the velocity uncertainties from GMOS and Hectospec are probably underestimated (see §7.3).

7.2   Duplicates from different spectrographs

There exist 67 GCs in common between the DEIMOS and GMOS catalogues. This sample has $\langle v_D - v_G \rangle = -0.6$ km s^{-1}, and the root-mean-square is rms= 23 km s^{-1}.

The DEIMOS and Hectospec samples have 21 GCs in common. The average velocity difference is $\langle v_D - v_H \rangle = 9.3$ km s^{-1}, with a scatter of rms= 30 km s^{-1}.

Lastly, we compare the GMOS and Hectospec catalogues. In this case the average velocity difference is $\langle v_H - v_D \rangle = -6$ km s^{-1}, with rms= 43 km s^{-1}. In the bottom panel in Figure 8 it is clear that some of the 25 objects in common between these two catalogues, scatter up to 5σ from each other.

7.3   Calibration of velocity uncertainties

By comparing radial velocities from different instruments we have seen that the average velocity difference is generally small (< 15 km s^{-1}), comparable to our DEIMOS uncertainties. However, the large scatter in $\langle \Delta v \rangle$ compared to the small error bars of the single datapoints, implies that the velocity uncertainties of GMOS and Hectospec catalogues are probably underestimated with respect to those of DEIMOS. Therefore, we need to re-normalize the velocity uncertainties of the first two spectrographs to those of DEIMOS.

We follow the method of Strader et al. (2011), and we mul-

tiply the uncertainties of the GMOS and Hectospec by a factor τ until the χ^2 difference between the velocities of the two catalogues is $\chi^2 \sim 1$. This normalization counts as a first-order correction to the velocity inconsistencies discussed above. We find that GMOS uncertainties need to be inflated by a factor of $\tau = 1.6$ with respect to DEIMOS. Once the uncertainties have been normalized, we weight-average the radial velocities of the GCs in common and we add the unique GMOS GCs to the DEIMOS catalogue. No rigid velocity offset has been applied to the GMOS velocities, as this is negligible ($\langle v_D - v_D \rangle = -0.6 \, \text{km s}^{-1}$).

Next, we compare the combined DEIMOS+GMOS catalogue to Hectospec. We renormalize the uncertainties of the Hectospec GCs by a factor of $\tau = 2.4$. Also in this case the velocity difference between the two datasets is negligible $\Delta v = 5 \, \text{km s}^{-1}$, therefore no offset is applied. We merge Hectospec to the master catalogue following the above procedure. Our master catalogue is composed of 447 spectroscopically confirmed stellar objects (GCs, UCDs and dwarf galaxies).

8 BUILDING UP THE SPECTROSCOPIC MASTER CATALOGUE

Before proceeding, we assign photometric measurements (i.e. magnitudes and sizes) to all confirmed objects. We match the position of confirmed GCs with *all* sources, both point-source and extended, extracted from ground based and HST imaging. We transform the ground based colours of the confirmed GCs from $(g-i)$ to $(g-z)$ using Equation 2. This is more convenient than transforming $(g-z)$ to $(g-i)$ because 60 per cent of the confirmed GCs have ACS photometry.

8.1 Clipping GCs from neighbour galaxies

The large field-of-view of Hectospec allows us to confirm GCs in some galaxies near NGC 4649 (see Figure 1). These GCs are treated as interlopers because they do not follow the gravitational potential of NGC 4649. The galaxies which may contaminate our sample are (from Cappellari et al. 2011): NGC 4621 ($v_{sys} = 467 \, \text{km s}^{-1}$), NGC 4638 ($v_{sys} = 1152 \, \text{km s}^{-1}$), NGC 4647 ($v_{sys} = 1409 \, \text{km s}^{-1}$, from NED), NGC 4660 ($v_{sys} = 1087 \, \text{km s}^{-1}$). We remind the reader that NGC 4649 has $v_{sys} = 1110 \, \text{km s}^{-1}$ (Cappellari et al. 2011).

Of the 7 GCs around NGC 4621, five are probably associated with this galaxy because their radial velocities are very similar to that of this galaxy as we will show in Section 9. The remaining two GCs (those in the NGC 4649 direction) have radial velocities consistent with NGC 4649 and they probably belong to this galaxy. Using geometrical criteria, we find 4 GCs associated with the elliptical galaxy NGC 4660.

We flag one GC as a member of NGC 4638 because it is very close to the center of this galaxy. However, the membership of this GC is impossible to confirm because the systemic velocity of NGC 4638 is almost identical to that NGC 4649.

GCs belonging to the spiral galaxy NGC 4647 (2.6 arcmin from NGC 4649) may also contaminate our GC sample. However, Strader et al. (2012) estimated that only ~ 10 objects in their GC catalogue are actually associated with NGC 4647. From our spectroscopic GC catalogue, we exclude one GC because of its proximity to NGC 4647 and because the spiral arms compromise the photometry of this object.

8.2 Clipping surrounding galaxies

In addition to GCs, we also measured radial velocities for some dwarf galaxies in the field.

With DEIMOS and GMOS, we observed the dE VCC 1982 ($v = 945 \pm 4 \, \text{km s}^{-1}$) and the nucleated dE VCC 1963 ($v = 1090 \pm 13 \, \text{km s}^{-1}$). For comparison, Lee et al. (2008) found velocities of $976 \pm 42 \, \text{km s}^{-1}$ and $1027 \pm 53 \, \text{km s}^{-1}$, respectively. We also obtained a radial velocity for a very low surface brightness nucleated dEs (ID 81 from Sabatini et al. 2005). We found its radial velocity to be $v = 1186 \pm 22 \, \text{km s}^{-1}$.

With Hectospec, we observed two dwarf galaxies present in the photometric catalogue of Grant et al. (2005). The first, is the nucleated dE VCC 1951, for which we find $v = 1089 \pm 32 \, \text{km s}^{-1}$, consistent with the measurement from SDSS DR10 $v = 1106 \pm 13 \, \text{km s}^{-1}$. The second, is the dE VCC 1986, for which we measure the redshift for the first time, finding $v = 850 \pm 37 \, \text{km s}^{-1}$.

The object M60-UCD1 is also treated as a galaxy and excluded from our sample (Strader et al. 2013).

One GC is only 7 arcsec away from a faint dwarf galaxy without spectroscopic confirmation, but we assume this is a projection effect and that these two objects are not physically connected. The same assumption was adopted for another GC which is ~ 8 arcsec away from the centre of a small galaxy without a redshift measurement (J124334.56+112727.3 from SDSS DR8).
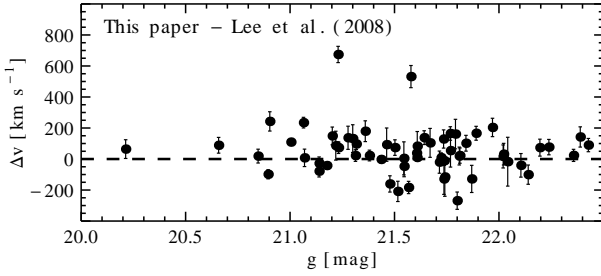
8.3 Additional GC datasets

We searched the SDSS archive for point sources with spectroscopic confirmation within 1 deg from NGC 4649. We found one unique object, which we added to our master catalogue, consistent with being a GC associated with NGC 4649 (ID SDSSJ124349.56+113810.3). We found four other GCs with SDSS spectroscopic confirmation, but these were not added to our catalogue because they already observed and confirmed with Hectospec.

Lee et al. (2008) published radial velocities for 93 GCs using CFHT/MOS with a median velocity uncertainty of $50 \, \text{km s}^{-1}$. Their observations explored an area $\approx 14 \times 14 \, \text{arcmin}^2$, which overlaps the spectroscopic observations from our paper. In fact, we found 61 GCs in common between our spectroscopic master catalogue and Lee et al.'s dataset. The median velocity difference is 38 km s^{-1}, with an rms of rms=$156 \, \text{km s}^{-1}$. A more careful inspection of the dataset, shown in Figure 9, reveals that the large rms value is driven by two objects (ID 201 and ID 226 using Lee et al. nomenclature) which scatter up to $600 \, \text{km s}^{-1}$ or (5σ) from the ideal $\Delta v = 0 \, \text{km s}^{-1}$ line. Removing these two extreme objects, the velocity difference rms decreases to $113 \, \text{km s}^{-1}$, still a factor of two larger than measured in our dataset.

The magnitude of this effect is comparable to that of the outliers found in M 87 by Strader et al. (2011) when comparing to the CFHT/MOS dataset of Hanes et al. (2001). We investigated the reason for this offset. We excluded mismatch because the outliers are not in overcrowded regions. We excluded a low signal-to-noise issue, because the two objects have intermediate magnitudes and because fainter duplicates have radial velocities in reasonable agreement with our dataset. As we could not identify the reason for this disagreement, we decided not to include the Lee et al. dataset in our DEIMOS catalogue because additional unknown outliers amongst the 32 unique Lee et al. GCs might skew our GC kinematic results.

Figure 9. Comparison with the data of Lee et al. (2008). The plot is the same as Figure 8, but for our combined spectroscopic master catalogue versus the CFHT/MOS GC dataset of Lee et al. (2008). Two objects scatter up to $700 \, \mathrm{km \, s^{-1}}$ with respect to the $\Delta v = 0$ dashed line.

9 OVERVIEW OF THE SPECTROSCOPIC CATALOGUE

We compile a list of 448 unique spectroscopically confirmed objects around NGC 4649. After clipping dwarf galaxies and GCs from neighbour galaxies, we are left with 431 unique GCs belonging to NGC 4649. The spectroscopic catalogue is given in Table 2. In the following, we review different projections of our parameter space, which involves photometric quantities (magnitude and colours) as well as physical quantities, such as the radial velocity and the physical size.

9.1 Spatial distribution

We start by looking at the positions on the sky of all confirmed objects (Figure 10). We confirm GCs up to 100 kpc from NGC 4649. DEIMOS and GMOS contribute to the GCs in the innermost 30 kpc, whereas all objects outside this radius are from Hectospec. In the outermost regions, mostly blue GCs are confirmed as expected from the shape of the GC surface density profile.
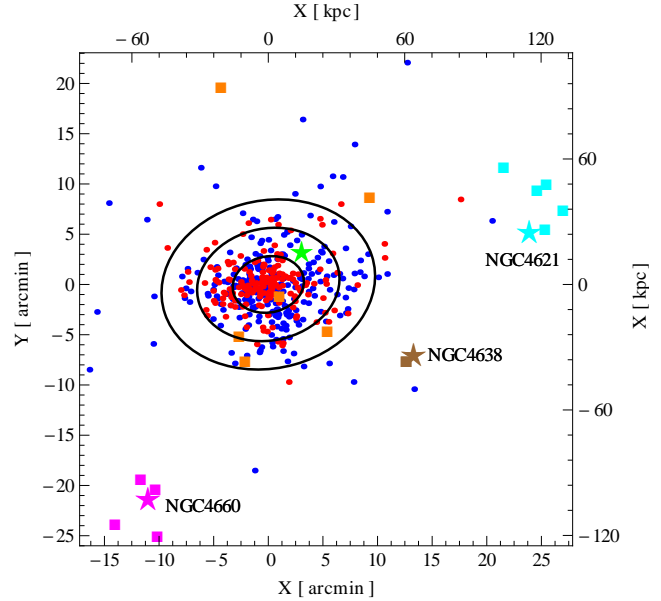
From Figure 10 is also clear that the GC systems of nearby galaxies are spatially separated from NGC 4649. Additional contamination from these galaxies is unlikely. The paucity of data in the immediate North-West of NGC 4649 is due to NGC 4647, which prevents us from detecting any source.

9.2 Globular cluster velocity distribution

In Figure 11 we plot the GC velocity distribution vs. galactocentric distance. This diagram is useful for identifying outliers which may scatter from the GC system velocity distribution. The latter is shown in the right panel of Figure 11. The skewness and kurtosis of the GC velocity distribution (excluding GCs from other galaxies) are $s = -0.05 \pm 0.11$ and $\kappa - 3 = -0.21 \pm 0.23$, respectively, suggesting Gaussianity. This is reassuring because we will invoke Gaussianity later on. If we consider only GCs within the innermost 100 arcsec, we estimate the systemic velocity of the GC system to be $v_{\mathrm{sys}} = 1115 \pm 28 \, \mathrm{km \, s^{-1}}$, very consistent with literature values for NGC 4649.

We bin the GCs by radius and calculate σ, which is the standard deviation of the binned velocities with respect to the systemic velocity of the galaxy. This allows us to draw a 3σ envelope as a tool to flag GCs deviating more than 3σ from the local GC velocity distribution. As can be seen in Figure 11, none of the objects shows such a deviation..

The velocity distribution of GCs is distinct from that of Galactic stars and from background galaxies. Therefore, a velocity cut at

Figure 10. Spatial distribution of the spectroscopically confirmed objects. NGC 4649 is at $(0, 0)$. Top and right axes show the co-moving physical scale at the distance of NGC 4649. Confirmed GCs are divided into blue and red subpopulations and coloured accordingly. The green star marks the position of NGC 4647. Orange boxes are dwarf galaxies discussed in the text. Ellipses are schematic isophotes at $3, 6, 9 \, R_e$. Position of some of the surrounding galaxies and their confirmed GCs are marked with coloured stars and squares, respectively. North is up, east is left.

$v = 400 \, \mathrm{km \, s^{-1}}$ ensures no contamination from Galactic stars. We note that for $R > 700$ arcsec, the majority of GCs have blue-shifted radial velocities. Within $R = 200$ arcsec, neither Galactic stars nor background galaxies were found thanks to the superior spatial resolution of ACS.. Confirmed GCs from other galaxies are clustered around the systemic velocity of the host galaxy.

9.3 Trends with colour

Figure 12 illustrates how some physical and photometric properties correlate with the observed GC colour. The quantities that we explore are the magnitude, the physical size r_h and the radial velocity v.
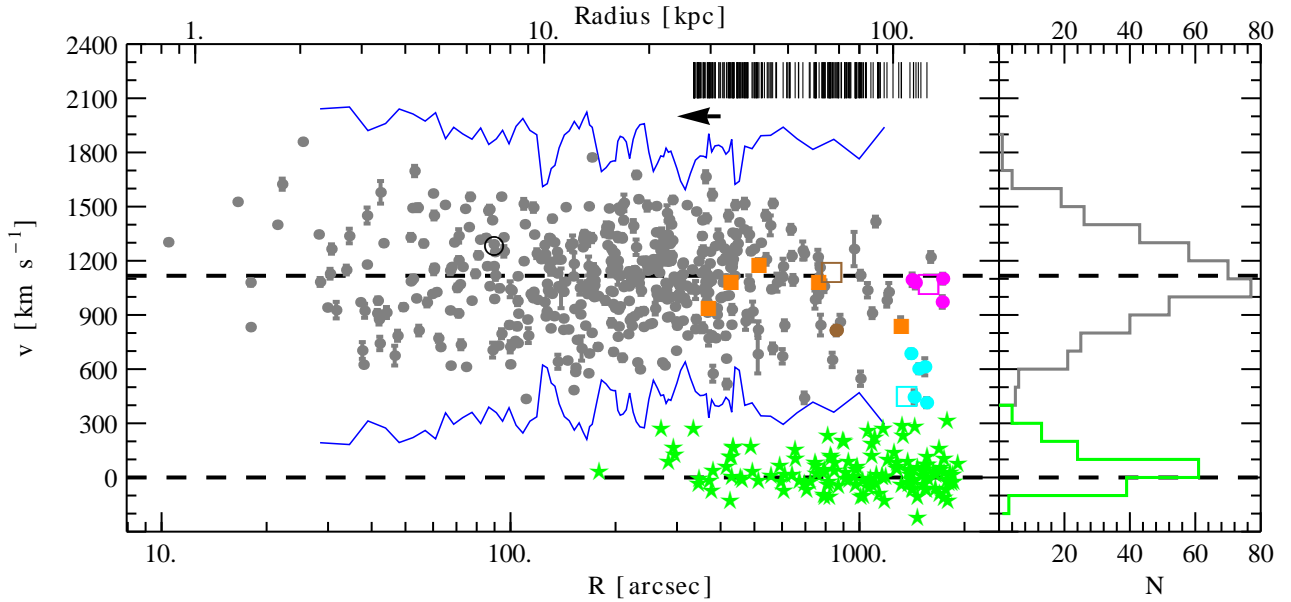
In the top panel we plot the colour histogram of all the *HST* candidates compared to the outcome of our spectroscopic follow-up. The overall colour distribution is well sampled with confirmed GCs. Bimodality is preserved, albeit there may be a deficit of redder GCs.

The correlation of colours with velocity (Panel *b*) suggests that the blue GCs scatter with respect to v_{sys} more than the red GCs. In other words, the velocity dispersion is larger than that of the red GCs. We will quantify this statement in the next section.

Panel *c* shows how colour correlates with size. The average GC size of the sample is $r_h \approx 2$ pc. We confirm 10 objects with $r_h > 10$ pc. We note that the catalogue of Strader et al. (2012) lists 22 objects with $r_h > 10$ pc, therefore our return rate is about 50 per cent. We confirm all three objects with $r_h > 20$ pc, two of which were already confirmed in Lee et al. (2008). The paucity of UCDs in this galaxy prevents us from any kinematic analysis of the UCD sample. We define UCDs as objects brighter than ω Cen and with $r_h > 10$ pc, where we have adopted the size cut adopted by Brodie et al. (2011) or Zhang et al. (2015).

ID	ID(S+12)	RA	DEC	$(g-z)$	z	R	v	δv
		[deg]	[deg]	[mag]	[mag]	[arcsec]	[km/s]	[km/s]
412	-	191.09555	11.45407	1.095	20.177	694	1240	32
295	-	190.85417	11.52163	0.991	20.455	237	1034	23
114	C4	190.94971	11.59446	1.140	19.943	197	1247	22
59	B12	190.92905	11.53665	1.574	19.759	75	612	6
339	-	191.04245	11.57867	0.948	18.483	420	1450	28
353	-	191.01315	11.61024	1.331	21.138	387	771	14
96	B87	190.97552	11.51810	1.361	21.552	233	1076	21
160	D28	190.90526	11.52134	0.948	20.352	129	1160	7
333	-	190.80938	11.57225	1.529	21.760	354	1424	8
295	-	190.85417	11.52163	0.991	20.455	237	1034	23
...	...	...	...	...	...	...	...	...

Table 2. Catalogue of the 431 spectroscopically confirmed GCs associated with NCG 4649. ID(S+12) is the ID of the GCs also present in Strader et al. (2012). Right ascension and declination are given in degrees. $(g-z)$ and z are either from Strader et al., or have been converted from gri magnitudes as described in §4.2. R is the galactocentric radius. v is the observed radial velocity of the objects. The quoted uncertainties on v, δv, have been re-normalized to the DEIMOS uncertainties (see text). The full table is available online.
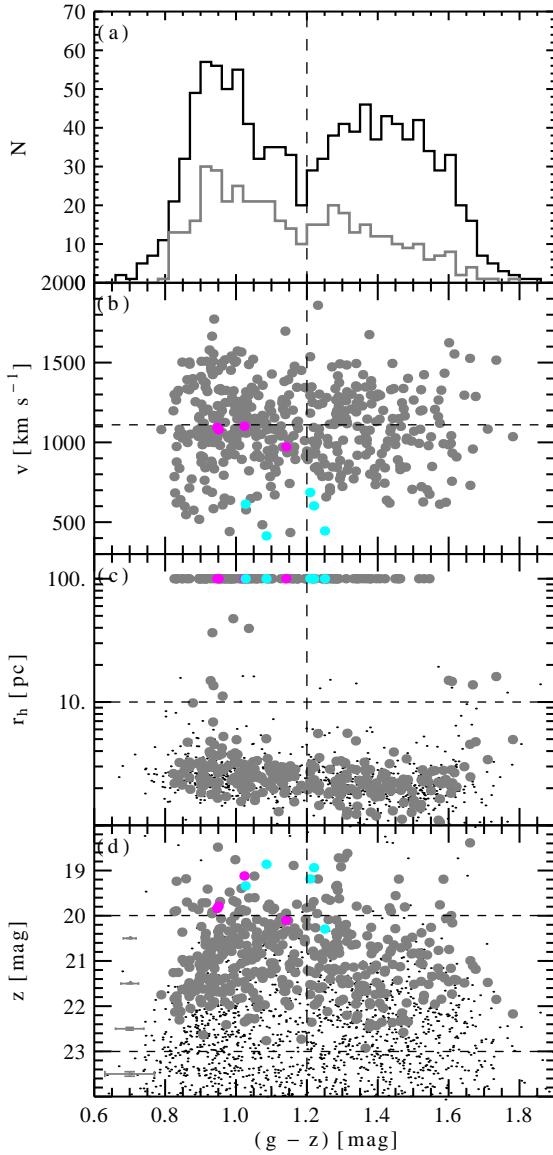

Figure 11. GC velocity distribution vs. galactocentric radius. Shown are all 447 spectroscopically confirmed objects. *Left panel:* observed radial velocities vs galactocentric distance R, shown in physical units on the top axis. Error bars are the velocity measurement errors re-normalized to the DEIMOS uncertainties (see text for details). Grey points are objects associated with NGC 4649; orange squares are the dwarf galaxies discussed in §8.2; the open black circle at $R \sim 100$ arcsec is the object M60-UCD1. Cyan points are GCs associated with NGC 4621; magenta points are GCs associated with NGC 4660; the brown point is a GC probably associated to NGC 4638. Open boxes show the position in this diagram of the three galaxies above. Green stars are Galactic stars. The $\pm 3\sigma$ envelope of the NGC 4649 GCs (grey points only) is shown as a blue lines. Horizontal lines show $v = 0 \, \text{km s}^{-1}$ and $v = v_{\text{sys}} = 1110 \, \text{km s}^{-1}$, which is the adopted systemic velocity of NGC 4649. Vertical thin black lines show the position of confirmed background galaxies with arbitrary velocities. *Right panel:* velocity distribution histogram for GCs/UCDs belonging to NGC 4649 only (grey histogram), and Galactic stars (green histogram). Both histograms have the same bin-step of $100 \, \text{km s}^{-1}$. GCs/UCDs are well separated from Galactic stars and background galaxies at all radii.

It is interesting that very extended objects are either the reddest, or the bluest. Among the blue objects, only 2 can be defined as "classic" UCDs, because along with being larger than GCs, they are also bright ($M_z < -11.0$ mag). The remaining blue objects have intermediate magnitudes and are the faint UCDs discussed in Brodie et al. (2011). Regarding the confirmed extended objects with red colours (four in total), these are generally fainter than $z > 21$, and never larger than $r_h = 20$ pc. These objects are more likely linked to faint-fuzzies (Brodie & Larsen 2002).

Lastly, the bottom panel shows the colour-magnitude diagram

of both candidate and confirmed GCs. We notice that some are brighter than ω Cen (see also Figure 3). The M60-UCD1 object has $z = 15.6$ mag and is not visible in the plot. The blue-tilt is clearly visible, as well as the fact that the red subpopulation has a larger colour spread compared to the blue subpopulation. We note the presence of ~ 10 objects with $z < 20$ mag and unusually blue colours $(g-z) < 0.95$ mag, which are found outside the ACS field-of-view and therefore lack of size information. It will be interesting to determine why these objects do not tilt towards redder

Figure 12. GC trends with colour. Each panel shows the $(g - z)$ colours of the spectroscopically confirmed GCs (large grey points) and of the *HST* GC catalogue (small black points). Coloured points are confirmed GCs from other galaxies as defined in Figure 11. The vertical line marks the separation between blue (on the left) and red GCs (on the right). Objects with ground-based photometry lack size measurements, and they were given $r_h = 100$ pc, as can be seen in Panel *(c)*. The black and grey histograms in Panel *(a)* are the HST dataset and the confirmed GCs, respectively; the horizontal line in Panel *(c)* separates UCDs from GCs; the horizontal lines in Panel *(d)* are the magnitude of ω Cen at the distance of NGC 4649 and the turn-over-magnitude.

colours like to bulk of blue GCs. We defer such analysis to a future paper.

10   KINEMATICS

So far, we have qualitatively discussed some properties of the spectroscopic sample, with no assumptions about the shape of the GC velocity distribution. This has suggested that blue and red GCs have different properties, as found in other GC systems (e.g.,

Schuberth et al. 2010a; Pota et al. 2013). We now quantify these findings and we derive physical quantities capable of characterizing the kinematics of the NGC 4649 GC system. We are interested in its rotation amplitude $v_{\rm rot}$, velocity dispersion σ, kinematic position angle θ_0, and root-mean-square velocity dispersion $v_{\rm rms}$.

10.1   Method

We start by calculating the root-mean-square velocity dispersion profile $v_{\rm rms}$, which measures the standard deviation of GC radial velocities from the systemic velocity of the galaxy:

$$v_{\rm rms}^2 = \frac{1}{N} \sum_i^N (v_i - v_{\rm sys})^2 - (\Delta v_i)^2 \qquad (3)$$

where Δv_i is the measurement uncertainty of the i-th GC. Uncertainties on $v_{\rm rms}$ are obtained using the formula of Danese et al. (1980). The $v_{\rm rms}$ can be thought of a measure of the specific kinetic energy of a system $v_{\rm rms}^2 \approx v_{\rm rot}^2 + \sigma^2$ and does not require any assumption about the detailed velocity distribution of the sample. However, we are also interested in the relative weights of $v_{\rm rot}$ and σ in the final value of $v_{\rm rms}$, which cannot be deduced from equation 3.

Therefore, in order to estimate σ, $v_{\rm rot}$ and $PA_{\rm kin}$, we adopt a model for the GC kinematics. This approach comes at the cost of assuming that the line-of-sight velocity distribution is Gaussian, but we have shown that this is a reasonable assumption to a first approximation.

We use the rotation model (Côté et al. 2001; Proctor et al. 2009):

$$v_{\rm mod} = v_{\rm sys} \pm \frac{v_{\rm rot}}{\sqrt{1 + \left(\frac{\tan(PA - PA_{\rm kin})}{q}\right)^2}} \qquad (4)$$

where $v_{\rm rot}$ is maximum amplitude of the sine curve; σ is the standard deviation of the data points with respect to $v_{\rm mod}$; the signs $+$ and $-$ are applied if the PA lies inside or outside the range $(\theta - \theta_0) = [-\pi/2, +\pi/2]$, respectively; $q = 0.84$ is the axial ratio of the GC system, assumed to be the same as that of NGC 4649.

To find the set of $(v_{\rm rot}, \sigma, PA_{\rm kin})$ that best reproduces the data, we minimize the log-likelihood function (i.e. the χ^2 function) (Bergond et al. 2006; Strader et al. 2011):

$$\chi^2 = \sum_i \frac{(v_i - v_{\rm mod})^2}{\sigma^2 + (\Delta v_i)^2} + \ln[\sigma^2 + (\Delta v_i)^2] \qquad (5)$$

where σ is the standard deviation of the datapoints with respect to the model.

Uncertainties are derived with "bootstrapping". We randomize the sample of interest 1000 times and we fit the data with equations 4 and 5 each time. We then infer the 68 per cent (1σ) error from the cumulative distribution function of each free parameter.

10.2   Independent tracers: stars and planetary nebulae

It is interesting to compare our GC kinematics results with those from two independent kinematic tracers: diffuse starlight from Foster et al. (2015) and planetary nebulae (PNe, Teodorescu et al. 2011).

The stellar data extend out to $2R_e$. We do not compare our results with long-slit or integral-field-unit data because these extend out to $\sim 0.5R_e$ and they do not overlap with our GC data in the innermost regions.

The PNe dataset consists of 298 objects. The PN that is furthest from the galaxy centre is at 400 arcsec, which corresponds to the radial extent of the DEIMOS GC sample. We infer the kinematics of PNe using equations 3 and 4, as done for GCs. Following Teodorescu et al. (2011), an average measurement uncertainty $\Delta v = 20\,\mathrm{km\,s^{-1}}$ is assumed for all PNe.

The kinematics and spatial distributions of stars and PNe have been shown to be similar (Coccato et al. 2009; Napolitano et al. 2009) because they are different manifestations of the same stellar population. It is less clear how the properties of PN systems generally compare with those of the GC system within the same galaxy (Woodley et al. 2010; Foster et al. 2011; Forbes et al. 2012; Pota et al. 2013; Coccato et al. 2013).

11 KINEMATIC RESULTS

We divide our sample into two subsamples. The "GC" sample is made by objects with $i > 20$ mag. We also require sizes $r_h < 10$ pc for the blue GCs ($(g - z) < 1.2$), if available, and $r_h < 20$ pc for the red GCs in order to include faint-fuzzies as part of the red GC sample. This choice is motivated by the findings that faint fuzzies are associated with galaxy disks (Chies-Santos et al. 2013; Forbes et al. 2014), although it is unclear if NGC 4649 possesses an embedded disk, as we discuss in Section 12. If physical sizes are not available, the object is still included in the GC sample if the magnitude criterion is satisfied. This GC sample includes classic GCs fainter than ω Cen, reflecting our attempt to prune from the sample extended objects without size measurements, but it may also include faint extended objects with no size measurements. The "bright" sample includes objects with $z < 20$ mag with no constraints on the size, and represents bright GCs and UCDs.

Each group is divided into blue and red GCs adopting a conservative colour cut at $(g - z) = 1.2$ mag. This choice introduces mixing between the two GC subpopulations for $(g-z) \sim 1.2 \pm 0.1$ mag. Therefore, we also investigate the effects of the colour cut on the results by selecting blue GCs with $(g-z) < 1.1$ mag and red GCs with $(g-z) > 1.3$ mag, respectively.
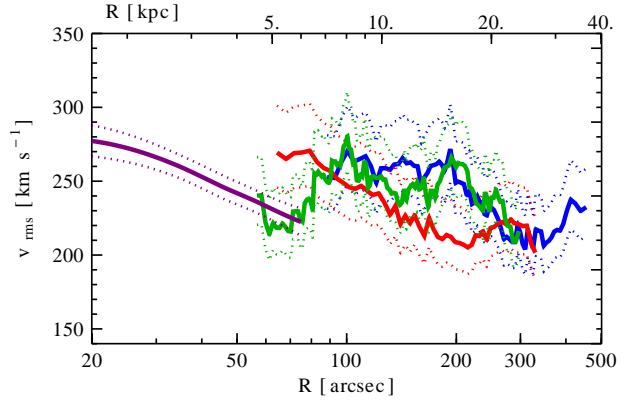
We start with a sample of 431 GCs. We exclude one isolated GC at 1500 arcsec from NGC 4649, and one GC because of its proximity to a bright star, which affects the magnitude measurements. In summary, we analyse the kinematics of a sample of 429 objects around NGC 4649.

11.1 The rms dispersion profile

We compute the GC v_{rms} velocity dispersion profile in radial bins with roughly 50 objects per bin. For the stars, we compute $v_{\mathrm{rms}}^2 = v_{\mathrm{rot}}^2 + \sigma^2$, using the tabulated values from Foster et al. (2015).

We calculate v_{rms} for GCs and PNe in rolling radial bins with 50 objects per bin. The results are shown in Figure 13. The v_{rms} profiles from the three tracers are diverse. The red GC v_{rms} profile decreases monotonically with radius, whereas the v_{rms} profile of blue GCs and PNe are bumpy and akin to each other, which is unexpected when compared to other galaxies.

We also note that the PNe results agree with the stellar v_{rms} profile in the region of overlap. On the other hand, the results for the red GCs seem to be systematically larger compared to the stars. It is unclear if this effect is real, or is due to unknown systematics in the spectroscopic measurements (e.g., Arnold et al. 2011). This result is still significant when a more extreme GC colour cut is adopted.

Figure 13. Root-mean-square velocity profile of kinematic tracers in NGC 4649. Shown as think lines are the rolling-binned v_{rms} profiles (equation 3) for blue and red GCs coloured accordingly, respectively. PNe results are shown in green. Stellar data are shown in purple. Dashed lines are 1σ envelopes.

11.2 Results from the kinematic modelling

The best fit parameters to eq. 4 for GCs and PNe sample (without any radial binning) are given in Table 3. GCs from surrounding galaxies are discarded from the analysis.
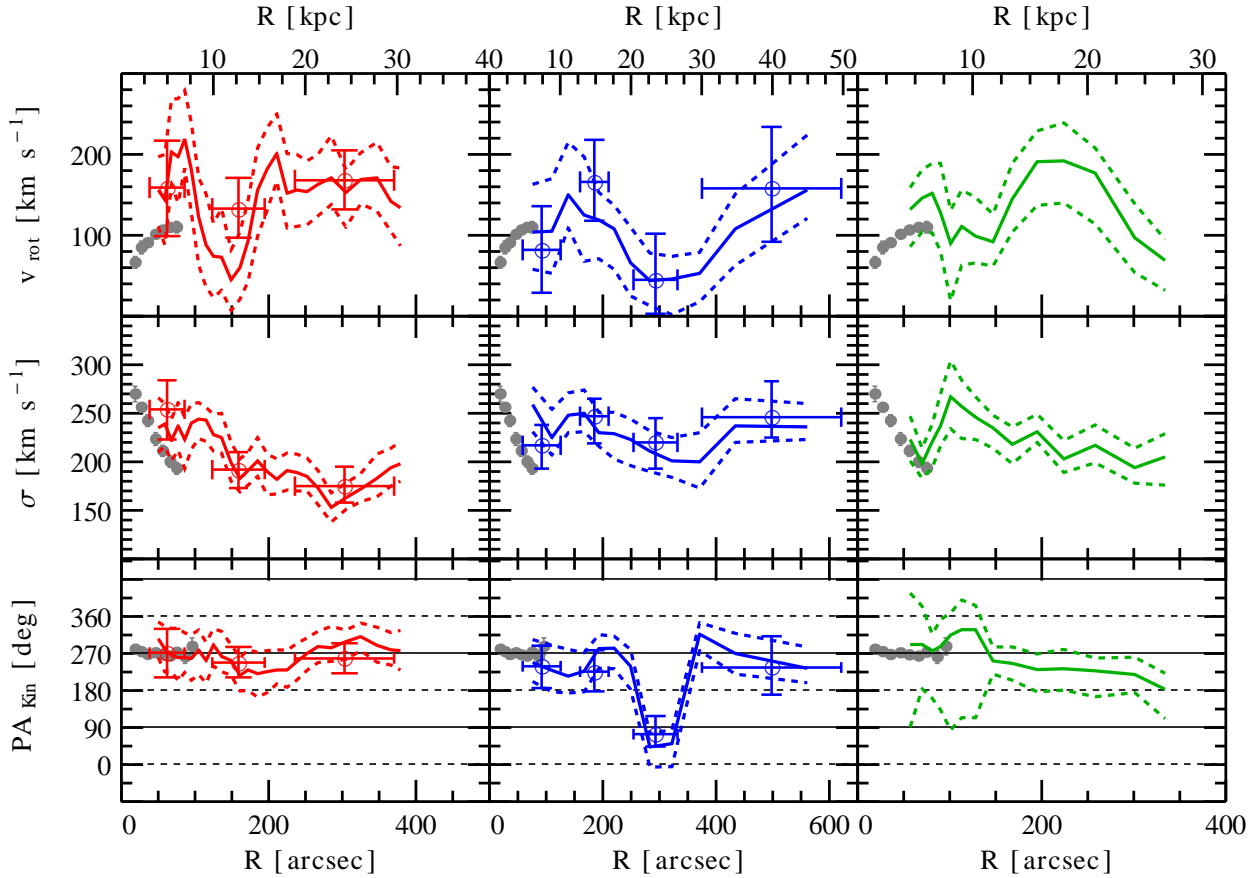
11.2.1 Kinematic radial profiles

Radial kinematic profiles for GCs, PNe and stars, are shown in Figure 14. We show running average profiles, with ~ 40 GCs per bin. Focusing on the red GCs (left panels), this sample shows a nearly constant rotation with radius. The rotation axis is very consistent with the photometric major axis of the galaxy ($PA_{\mathrm{kin}} \approx 270$ deg). The velocity dispersion is bumpy and decreases with radius. The dip in rotation velocity between 100 and 200 arcsec is intriguing and it will require future in-depth analysis. One possibility is that this feature is spurious because it occurs in the radial range where the spiral galaxy NGC 4647 prevents us from detecting GCs, therefore biasing the kinematic fit (see also Figure 10). Alternatively, the velocity dip may be real and linked to the recent interaction between NGC 4649 and the galaxy remnant M60-UCD1 (Seth et al. 2014), which lies at about 90 arcsec (7.2 kpc) along the minor axis of NGC 4649.

The blue GCs (middle panels) also show hints of rotation at all radii. The rotation amplitude is lower with respect to the red GCs. As with the red GCs, the rotation direction is generally consistent with the major axis of the galaxy. Minor axis counter-rotation is also detected at 300 arcsec. The velocity dispersion is constant at $\sigma = 240 \pm 30\,\mathrm{km\,s^{-1}}$, and higher than that of the red GCs, as found in other galaxies. The GC kinematic results are generally independent of the colour cut, as shown by the open points in Figure 14.

Lastly, the PNe (right panels) show a nearly constant rotation profile, but the kinematic position angle twists with radius, as found by Coccato et al. (2013). The velocity dispersion profile overlaps nicely with the stellar results in the innermost regions. We see a σ-bump at 100 arcsec, and a declining velocity dispersion profile intermediate between the results for the blue and red GCs.

Figure 14 shows that the three kinematic tracers are similar to each other in some aspects, e.g., rotation axis and rotation amplitude, but their velocity dispersions behave very differently. The

Figure 14. Kinematic radial profiles. Red, blue and green lines represent red GCs, blue GCs and PNe respectively. Open circles are the results for the reddest and the bluest GCs, respectively (see text). Grey points are stellar data from Foster et al. (2015). Each panel represents a solution to equation 4 for a given kinematic tracers. From the top to the bottom we show the rotation velocity $v_{\rm rot}$, the velocity dispersion σ with respect to $v_{\rm rot}$, and the kinematic position angle $PA_{\rm kin}$. Rotation occurs near the major axis at $PA \sim 270$ deg (marked with a black line). The dashed line indicates rotation along the minor axis. Running averages are performed with ~ 35, 40, 45 objects bin for red GCs, PNe and blue GCs, respectively. The co-moving step is 5 objects. Rotation along the major axis is detected at all radii.

sample size of the bright group is too low to compute radial profiles. However, the azimuthally averaged quantities from Table 3 indicate no significant difference between this group and the results discussed above.

11.2.2 Kinematic colour profiles

We have shown that the kinematic modelling results are not very sensitive to the assumed colour cut. We now bin the data by colour, rather than by galactocentric radius, and measure the azimuthally averaged kinematics of the objects within a certain colour bin. This exercise is independent of the colour cut. The results are shown in Figure 15 in the form of co-moving bins with 50 objects per bin. Comparison with the colour GC gradients in Figure 6 and Figure 14 is informative.

The results in Figure 15 show a double-peaked rotation pattern corresponding to the rotation of the blue and red GCs. The central panel shows a declining velocity dispersion in the range $0.8 < (g-z) < 1.0$ mag, which flattens at redder colours. More interestingly, the GCs with $(g-z) > 1.55$ mag have a large velocity dispersion and negligible rotation, because they are very centrally concentrated (see Figure 6). The rotation is consistent with the photometric major axis of the galaxy. On the other hand, minor axis ro-

tation is suggested for a group of blue GCs with $(g-z) \sim 0.9 \pm 0.1$ mag, as detected at intermediate radii (Figure 14).
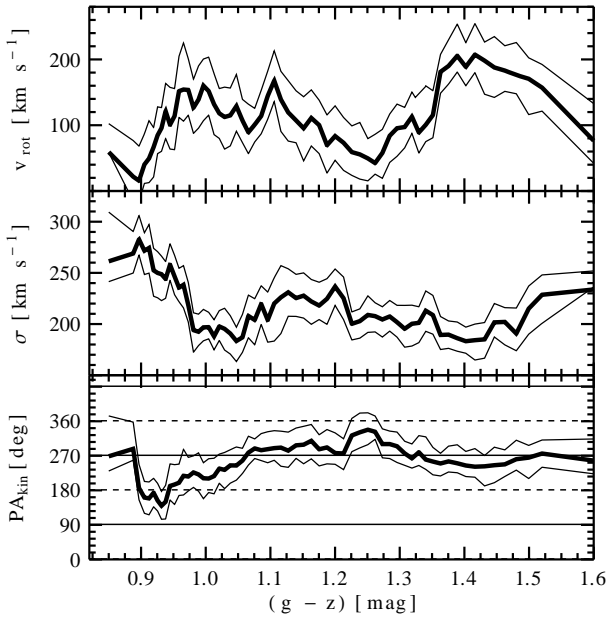
12 DISCUSSION

NGC 4649 is a normal looking elliptical galaxy with a relatively normal GC system. From a photometric point of view, we have shown that the GC system of NGC 4649 presents typical features seen in other elliptical galaxies of similar mass. We confirm statistically significant GC colour bimodality, as found in earlier work on NGC 4649 (Bridges et al. 2006; Pierce et al. 2006; Lee et al. 2008; Faifer et al. 2011; Chies-Santos et al. 2011). The GC specific frequency within 50 kpc $S_N = 3.5 \pm 0.1$ (Faifer et al. 2011) is consistent with values obtained for galaxies of similar mass (Peng et al. 2008). The two GC subpopulations have different spatial distributions (with the blue GCs being more extended than the red GCs) and negative colour gradients in the innermost regions.

From a kinematic point of view, the GC system of NGC 4649 is less normal when compared to other systems, because of the significant rotation detected at all radii for both GC subpopulations, which is a rare occurrence in elliptical galaxies of this mass. In what follows, we discuss possible formation scenarios for NGC 4649

Sample	N	$v_{\rm rot}$ [km s^{-1}]	σ [km s^{-1}]	$PA_{\rm kin}$ [degree]
		GC sample with $(g-i) < 1.2$ and $(g-i) > 1.2$		
All	366	95^{+18}_{-17}	229^{+7}_{-8}	256^{+10}_{-11}
Blue	212	81^{+20}_{-30}	237^{+9}_{-10}	244^{+17}_{-12}
Red	154	113^{+23}_{-20}	216^{+8}_{-10}	269^{+15}_{-13}
		GC sample with $(g-i) < 1.1$ and $(g-i) > 1.3$		
All	279	115^{+17}_{-24}	229^{+8}_{-8}	246^{+13}_{-13}
Blue	170	88^{+28}_{-28}	238^{+12}_{-11}	231^{+14}_{-14}
Red	109	150^{+28}_{-26}	209^{+15}_{-14}	260^{+14}_{-11}
		Bright sample with $(g-i) < 1.2$ and $(g-i) > 1.2$		
All	60	68^{+57}_{-37}	273^{+22}_{-19}	271^{+56}_{-45}
Blue	35	61^{+55}_{-42}	261^{+35}_{-43}	144^{+72}_{-68}
Red	25	243^{+55}_{-66}	238^{+32}_{-38}	293^{+15}_{-17}
		PNe sample		
PNe	298	98^{+17}_{-20}	234^{+10}_{-9}	267^{+11}_{-14}

Table 3. Results of the kinematic modelling. Listed are the best fit parameters to eq. 4 for different sub-samples, each containing N objects.

Figure 15. Kinematics as a function of GC colour. Each rolling bin contains 50 GCs. 1σ envelopes are shown as thin lines. The solid and dotted lines indicate rotation along the major and minor axis, respectively. A colour cut at $(g-z) = 1.2$ mag is used to derive the kinematic radial profiles.

based on the results from this paper and additional data from the literature.

12.1 Comparison with simulations

We start by looking at the innermost stellar kinematics in NGC 4649. We use the tools given by Naab et al. (2014) to link the observed innermost stellar kinematics from ATLAS$^{\rm 3D}$ with simulated galaxies with known formation histories at $z = 0$. NGC 4649

is classified as fast-rotator by Emsellem et al. (2011), with parameter[2] $\lambda_e = 0.127$ within $1R_e$ and ellipticity $\epsilon_e = 0.156$. New extended stellar kinematics data from Foster et al. (2015), have shown that the value of λ rises up to 0.6 at 2.5 R_e, meaning that the galaxy becomes more and more rotation dominated in the outer regions. Moreover, we find that:

• The pixel-by-pixel values of V/σ (where V is the observed radial velocity) is weakly anti-correlated and correlated h_3 and h_4, respectively. The Pearson coefficients for the ATLAS$^{\rm 3D}$ data are $\rho_{V/\sigma,h_3} = -0.08$ and $\rho_{V/\sigma,h_4} = 0.24$. This is shown in Figure 16, where we show both ATLAS$^{\rm 3D}$ data and DEIMOS stellar data from Foster et al. (2015) within $1R_e$. The parameters h_3 and h_4 describe the shape of the line-of-sight velocity distribution within a given spaxel. The correlation with V/σ is indicative of axisymmetry or of the presence of a disk.
• The stellar velocity dispersion is peaked at the centre, and decreases with radius (see Figure 14).
• Isophotes are elliptical (not disky) and there is no evidence of an embedded stellar disc (Kormendy et al. 2009; Vika et al. 2012).

According to the recipe of Naab et al. (2014), galaxies with the above properties formed via one late ($z < 1$) gas-poor major merger and many more minor mergers. Major mergers here are meant as those with up to 1:4 mass-to-mass ratio. Less than 18 per cent of the stellar mass formed in-situ, owing to the relatively low amount of gas involved in the merger. The remaining mass fraction, the one which makes up most of the stellar halo, was accreted via minor mergers. The strength of the correlation between h_3, h_4 and V/σ can be linked to the amount of gas involved in the merger (Hoffman et al. 2009). However, the observed correlations in Figure 16 are not strong, and therefore we cannot constrain the amount of gas, if any, involved in the major merger.
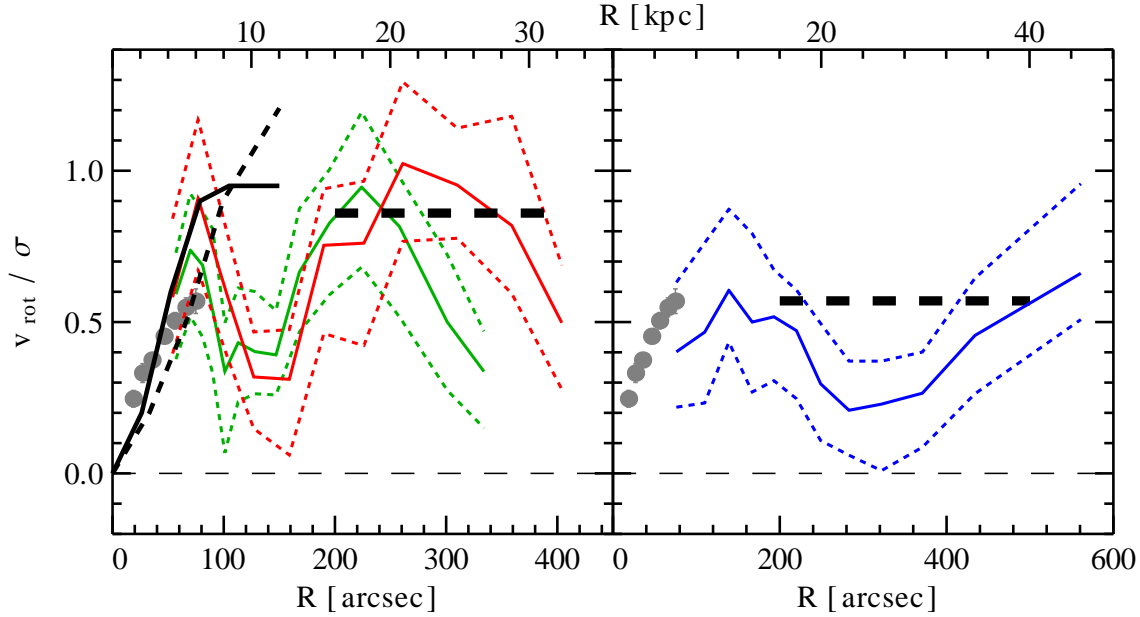
In principle, the observational properties listed above are also compatible with a gas-rich major merger remnant, but these remnants are usually less massive than $\log M_* = 11.3 M_\odot$ and they have disky isophotes, whereas NGC 4649 has $\log M_* = 11.7 M_\odot$ (Cappellari et al. 2013) and no strong evidence for a stellar disk (Vika et al. 2012). Spectral energy distribution fitting of NGC 4649 implies an average stellar age of 9.5 Gyr, no recent star formation and negligible gas content (Amblard et al. 2014).

Further evidence supporting a dry major merger formation pathway for NGC 4649 comes from the deficit of stellar mass ($M_{\rm def}$) at the centre (Lauer et al. 2005; Kormendy et al. 2009). The interaction between two supermassive black holes (SMBHs) during a dry merger can evacuate stars from the central regions of the galaxy (Merritt 2006). If the mass of the SMBH of the merger remnant is known $M_{\rm SMBH}$, the value of $M_{\rm def}$ can be connected to the number N of dry mergers that a galaxy has undergone, such that $M_{\rm def}/M_{\rm SMBH} \approx 0.5$ per merger. Dullo & Graham (2014) inferred $M_{\rm def}/M_{\rm SMBH} = 1.22$ for NGC 4649, meaning that this galaxy underwent the equivalent of ≈ 2.5 dry major mergers during its assembly, in general agreement with the predicted merger rate of galaxies with comparable stellar mass (Conselice & Arnold 2009; Khochfar et al. 2011; Naab et al. 2014).
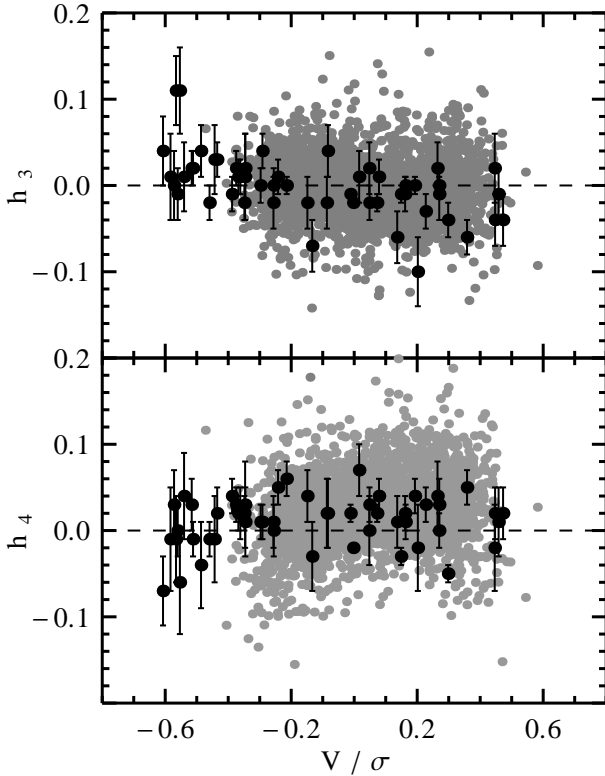
In summary, formation via dry major mergers and accretion can qualitatively reconcile the central stellar kinematic profiles with predictions from galaxy formation simulations. We now consider

---

[2] λ_e is a proxy for the galaxy angular momentum within $1\ R_e$ and it is equivalent to the luminosity weighted ratio $(v_{\rm rot}/\sigma)$ (Emsellem et al. 2007).

Figure 17. Ratio of the rotation amplitude over velocity dispersion as a function of galactocentric distance. GC data are for the classic GC sample only (i.e. from §11.2.1 and Figure 14). The left and right panels show the red GCs plus PNe (in green), and blue GCs respectively. Stellar data are shown in both panels as small grey points. The thin dashed line and the thin solid line are the (v_{rot}/σ) predicted in a 1:1 dissipationless merger (Di Matteo et al. 2009a) and 1:3 dissipative merger (Cretton et al. 2001), respectively. Thick dashed lines are the maximum (v_{rot}/σ) predicted in the 1:1 dissipationless merger simulations of Foster et al. (2011) (model 4 in their Table C1).

Figure 16. Pixel-by-pixel correlations between V/σ and h_3 and h_4. Gray points are ATLAS^{3D} data, whereas black points are DEIMOS stellar data within 1 R_e.

whether this picture is also consistent with the GC constraints discussed in this paper.

As discussed above, rotation in elliptical galaxy outskirts can be interpreted as the dynamical imprint of a major merger between two rotating disk progenitors (Côté et al. 2001; Cretton et al. 2001; Vitvitska et al. 2002; Bekki et al. 2005; Bournaud et al. 2007) or between two pressure-supported spheroids (Di Matteo et al. 2009a). The rotation of GCs (and other trace particles) in galaxy outskirts is also expected to have increased after a major merger (Bekki et al. 2005; McNeil-Moylan et al. 2012). This effect can be quantified through the ratio (v_{rot}/σ), which we show in Figure 17 for stars, GCs and PNe.

The left panel of Figure 17 shows that stars have an increasing (v_{rot}/σ) profile, whereas red GCs and PNe follow a bumpy pattern. We note that (v_{rot}/σ) is always < 1, and that the profiles seem to decline outside 20 kpc, which may indicate the turning point of the galaxy rotation curve. On the other hand, the blue GCs (right panel) have less rotation compared to other tracers, with a rising (v_{rot}/σ) profile at large radii.

Results for the stars are compared with the predicted (v_{rot}/σ) profile of a gas-rich major merger (Cretton et al. 2001) and of a gas-poor major-merger (Di Matteo et al. 2009a). Both simulations can reproduce the increasing stellar v_{rot}/σ profile in the region of overlap. The predicted v_{rot}/σ keeps rising with radius, whereas our data show a more irregular rise towards higher v_{rot}/σ.

Similarly, the v_{rot}/σ profile of GCs is compared with the dissipationless major mergers simulations from Foster et al. (2011) (thick lines in Figure 17). These simulations can qualitatively reproduce the maximum v_{rot}/σ of blue and red GCs results for a wide range of orbital configurations (see Table C1 in Foster et al. 2011). Therefore, the radial increase of v_{rot}/σ for the GC is qualitatively consistent with a dry major merger picture. We note

that kinematic predictions for GC kinematics in gas-rich major merger remnants are currently not available in the literature (Kruijssen et al. 2012).

Schauer et al. (2014) showed that major merger simulations predict that the velocity dispersion profile of the kinematic tracers of the remnant should be "bumpy" at intermediate radii. This is a permanent feature within the galaxy, and it has been observed in some systems (e.g., Pota et al. 2013). We find that the velocity dispersion of red GCs and PNe in NGC 4649 is bumpy, especially at ~ 100 arcsec (see Figure 14). By extrapolating the stellar velocity dispersion profile at large radii, we estimated that the bumps have an amplitude of ≈ 50 km s^{-1}, in general agreement with the predictions of Schauer et al. (2014).

It is known that a galaxy's metallicity profile can be continuously reshaped during its life cycle. Dissipative collapse tends to create steep metallicity radial profiles (Pipino et al. 2010), whereas major mergers can steepen or flatten metallicity gradients, depending on the initial conditions of the progenitors (Font et al. 2011). Similar results can also be achieved through dissipationless major mergers (Di Matteo et al. 2009b). Other processes, such as AGN feedback, known to have occurred in NGC 4649 (Paggi et al. 2014), can flatten the global metallicity profile because they quench star formation in the innermost regions (Hirschmann et al. 2014).

Given these continuous transformations of the metallicity profiles, a direct comparison between the observed colour profiles of stars and GCs with galaxy simulations is more uncertain. Dry major mergers (our favoured formation model so far) can leave the metallicity of the remnant unchanged if both progenitors have sufficiently steep metallicity gradients (Di Matteo et al. 2009b). In this context, the observed negative gradients in NGC 4649 could be interpreted as the pre-merger gradients of the progenitor galaxies, which remained unchanged after the merger. This assumes that the merger triggered no star formation and that the initial metallicity slopes of the progenitors were equally steep.

Our results show evidence of flat colour profiles outside 20 kpc, consistent with other studies (Rhode & Zepf 2001; Cantiello et al. 2007; Bassino et al. 2006; Forbes et al. 2011; Faifer et al. 2011; Liu et al. 2011). This feature is interpreted as the transition from the galaxy central part, created by dissipative processes, to an extended component made by secular accretion of (mostly metal-poor) satellite galaxies. In this context, GC bimodality is a natural manifestation of dual galaxy formation pathway (Côté 1999; Brodie et al. 2014): red GCs mostly form in-situ, along with bulk of stars, and are therefore more centrally concentrated. Blue GCs are mostly accreted and are therefore more extended (Tonini 2013).

The GC system of NGC 4649 is consistent with being old (> 10 Gyr; Chies-Santos et al. 2011). However, Pierce et al. (2006) found about four GC with very young ages in NGC 4649. These objects are listed in Table 4. From this Table, we can see that young GCs have all red colours, but the sizes are ordinary for normal GCs. Given the lack of recent star formation in NGC 4649, the existence of these young GCs could be explained if they formed along with their host satellite galaxy at $z \leqslant 1$ (Tonini 2013), which was then accreted onto NGC 4649.

Lastly, we note that NGC 4649 was classified as a galaxy with "subtle S0 attributes" (Sandage & Tammann 1981; Sandage & Bedke 1994). Processes such as secular evolution (Larson et al. 1980; Boselli & Gavazzi 2009; Kormendy 2013) or gas stripping (e.g., Moore et al. 1996; Lake et al. 1998; Chung et al. 2007) can both transform a gas-rich spiral galaxy into a gas-poor S0 (Kormendy & Bender 2012).

ID - ID(P+06)	Age [Gyr]	v [km s^{-1}]	$(g-z)$ [mag]	r_h [pc]	R [kpc]
J187 - 1443	2.1 ± 0.6	703 ± 46	1.53	2.52	3
A8 - 502	3.0 ± 0.8	705 ± 41	1.50	1.87	7
B36 - 175	2.4 ± 0.4	836 ± 11	1.392	1.95	16
B85 - 89	2.4 ± 0.8	1148 ± 16	1.29	2.10	18

Table 4. Properties of young GCs in NGC 4649. ID(P+06) and age are from Pierce et al. (2006). The ID, colour $(g - z)$ and size r_h are from (Strader et al. 2012). The velocity v is from this paper. Errors on $(g-z)$ and r_h are less than 10 per cent. R is the projected distance from NGC 4649.

However, galaxies thought to be faded spirals have the photometric stellar disk still in place (Cortesi et al. 2011; Forbes et al. 2012; Arnold et al. 2011; Cortesi et al. 2013; Kormendy 2013). No strong evidence for a stellar disk has been found in NGC 4649 (Vika et al. 2012; Kormendy 2013). Recently, Graham et al. (2015) pointed out that NGC 4649 is particularly difficult to decompose into bulge and disk. It was recently shown that gas-rich major mergers can also produce S0 remnants with embedded disks (Querejeta et al. 2014). Naab et al. (2014) predicts that these remnants have disky kinematics with rising or peaked $v_{\rm rot}/\sigma$ profiles, along with h_3 and h_4 strongly correlated with V/σ, which is not consistent with our findings.

12.2 Final remarks and the interaction with NGC 4647

We have shown that a formation pathway via a major merger between two gas-poor galaxies, combined with satellite accretion, can simultaneously explain both the inner stellar observations and the outer GC observations. After a major-merger, the angular momentum is transported to the outer regions of the remnant, explaining the high rotation velocity observed for stars, GCs and PNe.

If no gas was involved in the merger, the GC system of the primordial galaxies got mixed together, preserving their original metallicity gradients. Additional GCs (mostly metal-poor) are then accreted into the halo of the galaxy, explaining the extended spatial distribution of blue GCs. This scenario is supported by the presence of a depleted stellar core in the galaxy's innermost regions.

The possible interaction between NGC 4649 and NGC 4647, which is only 13 kpc away in projection, has been widely debated in the literature. A gri color image of this galaxy group is shown in Figure 18. Radio observations suggest that the morphology of CO and HI maps are mildly disturbed, and so are the corresponding velocity fields (Rubin et al. 1999; Young et al. 2006). However, radio observations alone do not return conclusive results on whether or not this galaxy pair is actually interacting. A similar conclusion was reached by de Grijs & Robertson (2006) from an analysis of ACS imaging of this galaxy. Moreover, the distribution of optical light around NGC 4647 and NGC 4649 shows no sign of disturbances (Figure 18). On the other hand, new observations found evidence for enhanced star formation in the region between NGC 4647 and NGC 4649 (Lanz et al. 2013; Mineo et al. 2014).

D'Abrusco et al. (2014) and Mineo et al. (2014) have suggested that the substructures in the 2D distribution of GCs from ACS imaging may reflect a recent interaction in NGC 4649, but the role of NGC 4647 is still unclear. No significant sign of ongoing interaction between NGC 4649 and NGC 4647 was observed in the 2D velocity field of the GCs (Coccato et al. 2013) based on the GC catalogue of Lee et al. (2008).

Our kinematic results show some interesting features, such as

Figure 18. Subaru/Suprime-Cam gri colour image of NGC 4649 (left) and NGC 4647 (right). The projected separation between the two galaxies is 13 kpc. There are no clear signs of interaction between the two galaxies. North is up, East is left.

wiggly velocity profiles, counter rotation, and a multi-spin PN system. We find that GCs with $(g - z) \approx 0.9 \pm 0.1$ mag, counter-rotate with respect to main rotation direction of the galaxy, which may represent the imprint of a recent interaction (Seth et al. 2014). Moreover, Pierce et al. (2006) found a handful of GCs only 2 Gyr old in NGC 4649, which may be linked to a recent accretion event. Similar kinematic anomalies, such as strong rotation amplitude and multi-spin features, have been found in GC systems of interacting early-type galaxies, such as NGC 4365 (Blom et al. 2012), and merger remnants like NGC 5128 (Woodley et al. 2010; Woodley & Harris 2011). Computer simulations may determine whether the kinematic features observed in NGC 4649 encode signatures of an ongoing interaction between NGC 4649 and NGC 4647. Based on these contrasting results, it appears that, if NGC 4647 and NGC 4647 are interacting, we are witnessing the very early stages of this interaction.

13 SUMMARY

In this paper, we have studied the globular cluster (GC) system of the massive elliptical galaxy NGC 4649 (M60). We combined wide-field spectroscopy with wide-field imaging from space-based and ground-based telescopes. We build up a photometric catalogue combining space-based *HST*/ACS data from Strader et al. (2012), ground-based archival CFHT/MegaCam, and new Subaru/Suprime-Cam data. GCs are selected based on colour and magnitude constrains. We detect all the photometric features usually seen in GC systems of large ellipticals: the GC system of

NGC 4649 is made up of two subpopulations: the red (metal rich) GCs are centrally concentrated. Their spatial distribution is consistent with that of the starlight and planetary nebulae in NGC 4649. The blue (metal poor) GCs are more extended. The colour gradients of blue and red GCs are flat outside 20 kpc, interpreted as evidence of accretion of metal-poor satellites into the stellar halo of NGC 4649.

The spectroscopic follow-up is performed with three multi-object spectrographs: Keck/DEIMOS, Gemini/GMOS and MMT/Hectospec. These cover different effective areas around NCC 4649, but they are complementary with each other. We confirmed 431 GCs associated with NGC 4649, plus some GCs from surrounding galaxies, and dwarf galaxies. The contamination from stars and background galaxies is consistent with zero. We analyse the kinematics of blue (60 per cent of the total sample) and red GCs (40 per cent), along with literature planetary nebulae data. Results are:

- Significant rotation at all radii is detected for stars, PNe and blue and red GCs. Rotation occurs preferentially along the major axis of the galaxy.
- The velocity dispersion of the three tracers look very different. Blue GCs and PNe have higher velocity dispersion in the outer regions, whereas the red GCs and the innermost PNe are consistent with the stellar kinematics and have lower dispersions.
- We report peculiar kinematic features for both GCs and PNe. The rotation axis of PNe twists with radius, whereas a group of blue GCs at intermediate radii counter-rotate with respect to the bulk of blue GCs. The velocity dispersion profiles are bumpy, a feature

which may indicate that this galaxy underwent major mergers in the past.

We discuss possible formation scenarios for this galaxy, contrasting stellar and GC observations with recent galaxy formation simulations. We find that a formation via dry (no gas) major-merger between two galaxies can, regardless of their initial angular momentum, consistently reproduce stellar observations in the innermost regions and GC observations in the outermost regions of NGC 4649. We consider the possibility that NGC 4649 was spiral galaxy which evolved in an elliptical galaxy because of gas stripping, but the apparent non-detection of the primordial disk in NGC 4649 makes this scenario unlikely. We find no strong evidence to support an upcoming interacting between NGC 4649 and the spiral NGC 4647.

ACKNOWLEDGEMENTS

REFERENCES

Amblard A., Riguccini L., Temi P., Im S., Fanelli M., Serra P., 2014, ApJ, 783, 135

Arnold J. A., Romanowsky A. J., Brodie J. P., Chomiuk L., Spitler L. R., Strader J., Benson A. J., Forbes D. A., 2011, ApJ, 736, L26
Arp H., 1966, ApJS, 14, 1
Ashman K. M., Bird C. M., Zepf S. E., 1994, AJ, 108, 2348
Atkinson A. M., Abraham R. G., Ferguson A. M. N., 2013, ApJ, 765, 28
Bassino L. P., Richtler T., Dirsch B., 2006, MNRAS, 367, 156
Bekki K., Beasley M. A., Brodie J. P., Forbes D. A., 2005, MNRAS, 363, 1211
Bergond G., Zepf S. E., Romanowsky A. J., Sharples R. M., Rhode K. L., 2006, A&A, 448, 155
Bertin E., Arnouts S., 1996, A&AS, 117, 393
Blom C., Forbes D. A., Brodie J. P., Foster C., Romanowsky A. J., Spitler L. R., Strader J., 2012, MNRAS, 426, 1959
Boselli A., Gavazzi G., 2009, A&A, 508, 201
Bournaud F., Elmegreen B. G., Elmegreen D. M., 2007, ApJ, 670, 237
Bridges T., Gebhardt K., Sharples R., Faifer F. R., Forte J. C., Beasley M. A., Zepf S. E., Forbes D. A., Hanes D. A., Pierce M., 2006, MNRAS, 373, 157
Brodie J. P., Larsen S. S., 2002, AJ, 124, 1410
Brodie J. P., Romanowsky A. J., Strader J., Forbes D. A., 2011, AJ, 142, 199
Brodie J. P., Romanowsky A. J., Strader J., Forbes D. A., Foster C., Jennings Z. G., Pastorello N., Pota V., Usher C., Blom C., Kader J., Roediger J. C., Spitler L. R., Villaume A., Arnold J. A., Kartha S. S., Woodley K. A., 2014, ApJ, 796, 52
Brodie J. P., Strader J., 2006, ARA&A, 44, 193
Cantiello M., Blakeslee J. P., Raimondo G., 2007, ApJ, 668, 209
Cappellari M., Emsellem E., Krajnović D., McDermid R. M., Scott N., Verdoes Kleijn G. A., Young L. M., Alatalo K., Bacon R., Blitz L., Bois M., Bournaud F., Bureau M., Davies R. L., 2011, MNRAS, 413, 813
Cappellari M., Scott N., Alatalo K., Blitz L., Bois M., Bournaud F., Bureau M., Crocker A. F., 2013, MNRAS, 432, 1709
Chies-Santos A. L., Cortesi A., Fantin D. S. M., Merrifield M. R., Bamford S., Serra P., 2013, A&A, 559, A67
Chies-Santos A. L., Larsen S. S., Kuntschner H., Anders P., Wehner E. M., Strader J., Brodie J. P., Santos J. F. C., 2011, A&A, 525, A20
Chies-Santos A. L., Larsen S. S., Wehner E. M., Kuntschner H., Strader J., Brodie J. P., 2011, A&A, 525, A19
Chung A., van Gorkom J. H., Kenney J. D. P., Vollmer B., 2007, ApJ, 659, L115
Coccato L., Arnaboldi M., Gerhard O., 2013, MNRAS, 436, 1322
Coccato L., Gerhard O., Arnaboldi M., Das P., Douglas N. G., Kuijken K., Merrifield M. R., Napolitano N. R., Noordermeer E., Romanowsky A. J., Capaccioli M., Cortesi A., de Lorenzi F., Freeman K. C., 2009, MNRAS, 394, 1249
Conselice C. J., Arnold J., 2009, MNRAS, 397, 208
Cooper M. C., Newman J. A., Davis M., Finkbeiner D. P., Gerke B. F., , 2012, spec2d: DEEP2 DEIMOS Spectral Pipeline, Astrophysics Source Code Library
Cortesi A., Merrifield M. R., Arnaboldi M., Gerhard O., Martinez-Valpuesta I., Saha K., Coccato L., Bamford S., Napolitano N. R., Das P., Douglas N. G., Romanowsky A. J., Kuijken K., Capaccioli M., Freeman K. C., 2011, MNRAS, 414, 642
Cortesi A., Merrifield M. R., Coccato L., Arnaboldi M., Gerhard O., Bamford S., Napolitano N. R., Romanowsky A. J., Douglas N. G., Kuijken K., Capaccioli M., Freeman K. C., Saha K., Chies-Santos A. L., 2013, MNRAS, 432, 1010
Côté P., 1999, AJ, 118, 406

Côté P., McLaughlin D. E., Cohen J. G., Blakeslee J. P., 2003, ApJ, 591, 850

Côté P., McLaughlin D. E., Hanes D. A., Bridges T. J., Geisler D., Merritt D., Hesser J. E., Harris G. L. H., Lee M. G., 2001, ApJ, 559, 828

Cretton N., Naab T., Rix H.-W., Burkert A., 2001, ApJ, 554, 291

D'Abrusco R., Fabbiano G., Mineo S., Strader J., Fragos T., Kim D.-W., Luo B., Zezas A., 2014, ApJ, 783, 18

Danese L., de Zotti G., di Tullio G., 1980, A&A, 82, 322

Das P., Gerhard O., Churazov E., Zhuravleva I., 2010, MNRAS, 409, 1362

Das P., Gerhard O., Mendez R. H., Teodorescu A. M., de Lorenzi F., 2011, MNRAS, 415, 1244

de Grijs R., Robertson A. R. I., 2006, A&A, 460, 493

Di Matteo P., Pipino A., Lehnert M. D., Combes F., Semelin B., 2009a, A&A, 499, 427

Di Matteo P., Pipino A., Lehnert M. D., Combes F., Semelin B., 2009b, A&A, 499, 427

D'Souza R., Kauffman G., Wang J., Vegetti S., 2014, MNRAS, 443, 1433

Duc P.-A., Cuillandre J.-C., Karabal E., Cappellari M., Alatalo K., Blitz L., Bournaud F., Bureau M., Crocker A. F., Davies R. L., Davis 2015, MNRAS, 446, 120

Dullo B. T., Graham A. W., 2014, MNRAS, 444, 2700

Ebrova I., 2013, ArXiv e-prints

Emsellem E., Cappellari M., Krajnović D., Alatalo K., Blitz L., Bois M., Bournaud F., Bureau M., Davies R. L., Davis T. A., de Zeeuw P. T., 2011, MNRAS, 414, 888

Emsellem E., Cappellari M., Krajnović D., van de Ven G., Bacon R., Bureau M., Davies R. L., de Zeeuw P. T., Falcón-Barroso J., Kuntschner H., McDermid R., Peletier R. F., Sarzi M., 2007, MNRAS, 379, 401

Faber S. M., Phillips A. C., Kibrick R. I., Alcott B., Allen S. L., Burrous J., Cantrall T., Clarke D., Coil A. L., Cowley D. J., Davis 2003, in Iye M., Moorwood A. F. M., eds, Instrument Design and Performance for Optical/Infrared Ground-based Telescopes Vol. 4841 of Society of Photo-Optical Instrumentation Engineers (SPIE) Conference Series, The DEIMOS spectrograph for the Keck II Telescope: integration and testing. pp 1657–1669

Fabricant D., Fata R., Roll J., Hertz E., Caldwell N., Gauron T., Geary 2005, PASP, 117, 1411

Faifer F. R., Forte J. C., Norris M. A., Bridges T., Forbes D. A., Zepf S. E., Beasley M., Gebhardt K., Hanes D. A., Sharples R. M., 2011, MNRAS, 416, 155

Ferrarese L., Côté P., Cuillandre J.-C., Gwyn S. D. J., Peng E. W., MacArthur L. A., Duc P.-A., Boselli A., Mei S., Erben 2012, ApJS, 200, 4

Font A. S., McCarthy I. G., Crain R. A., Theuns T., Schaye J., Wiersma R. P. C., Dalla Vecchia C., 2011, MNRAS, 416, 2802

Forbes D. A., Almeida A., Spitler L. R., Pota V., 2014, MNRAS, 442, 1049

Forbes D. A., Cortesi A., Pota V., Foster C., Romanowsky A. J., Merrifield M. R., Brodie J. P., Strader J., Coccato L., Napolitano N., 2012, MNRAS, 426, 975

Forbes D. A., Ponman T., O'Sullivan E., 2012, MNRAS, 425, 66

Forbes D. A., Spitler L. R., Strader J., Romanowsky A. J., Brodie J. P., Foster C., 2011, MNRAS, 413, 2943

Forte J. C., Faifer F., Geisler D., 2005, MNRAS, 357, 56

Foster C., Lux H., Romanowsky A. J., Martínez-Delgado D., Zibetti S., Arnold J. A., Brodie J. P., Ciardullo R., GaBany R. J., Merrifield M. R., Singh N., Strader J., 2014, MNRAS, 442, 3544

Foster C., Spitler L. R., Romanowsky A. J., Forbes D. A., Pota V., Bekki K., Strader J., Proctor R. N., Arnold J. A., Brodie J. P., 2011, MNRAS, 415, 3393

Foster et al. 2015, submitted

Graham A. W., Dullo B. T., Savorgnan G. A. D., 2015, ArXiv e-prints

Grant N. I., Kuipers J. A., Phillipps S., 2005, MNRAS, 363, 1019

Gwyn S. D. J., 2008, PASP, 120, 212

Hanes D. A., Côté P., Bridges T. J., McLaughlin D. E., Geisler D., Harris G. L. H., Hesser J. E., Lee M. G., 2001, ApJ, 559, 812

Harris W. E., Harris G. L. H., Alessi M., 2013, ApJ, 772, 82

Harris W. E., Harris G. L. H., Barmby P., McLaughlin D. E., Forbes D. A., 2006, AJ, 132, 2187

Hirschmann M., Naab T., Ostriker J. P., Forbes D. A., Duc P.-A., Davé R., Oser L., Karabal E., 2014, ArXiv e-prints

Hoffman L., Cox T. J., Dutta S., Hernquist L., 2009, ApJ, 705, 920

Hoffman L., Cox T. J., Dutta S., Hernquist L., 2010, ApJ, 723, 818

Hook I. M., Jørgensen I., Allington-Smith J. R., Davies R. L., Metcalfe N., Murowinski R. G., Crampton D., 2004, PASP, 116, 425

Humphrey P. J., Buote D. A., Brighenti F., Gebhardt K., Mathews W. G., 2008, ApJ, 683, 161

Hwang H. S., Lee M. G., Park H. S., Kim S. C., Park J.-H., Sohn Y.-J., Lee S.-G., Rey S.-C., Lee Y.-W., Kim H.-I., 2008, ApJ, 674, 869

Jordán A., Blakeslee J. P., Côté P., Ferrarese L., Infante L., Mei S., Merritt D., Peng E. W., Tonry J. L., West M. J., 2007, ApJS, 169, 213

Khochfar S., Emsellem E., Serra P., Bois M., Alatalo K., Bacon R., Blitz L., Bournaud F., Bureau M., Cappellari M., Davies R. L., Davis 2011, MNRAS, 417, 845

Kormendy J., 2013, Secular Evolution in Disk Galaxies. p. 1

Kormendy J., Bender R., 2012, ApJS, 198, 2

Kormendy J., Fisher D. B., Cornell M. E., Bender R., 2009, ApJS, 182, 216

Kruijssen J. M. D., Pelupessy F. I., Lamers H. J. G. L. M., Portegies Zwart S. F., Bastian N., Icke V., 2012, MNRAS, 421, 1927

Lake G., Katz N., Moore B., 1998, ApJ, 495, 152

Lanz L., Zezas A., Brassington N., Smith H. A., Ashby M. L. N., da Cunha E., Fazio G. G., Hayward C. C., Hernquist L., Jonsson P., 2013, ApJ, 768, 90

Larson R. B., Tinsley B. M., Caldwell C. N., 1980, ApJ, 237, 692

Lauer T. R., Faber S. M., Gebhardt K., Richstone D., Tremaine S., Ajhar E. A., Aller M. C., Bender R., Dressler A., Filippenko A. V., Green R., Grillmair C. J., Ho L. C., Kormendy J., Magorrian J., Pinkney J., Siopis C., 2005, AJ, 129, 2138

Leaman R., VandenBerg D. A., Mendel J. T., 2013, MNRAS, 436, 122

Lee M. G., Hwang H. S., Park H. S., Park J.-H., Kim S. C., Sohn Y.-J., Lee S.-G., Rey S.-C., Lee Y.-W., Kim H.-I., 2008, ApJ, 674, 857

Lee M. G., Park H. S., Kim E., Hwang H. S., Kim S. C., Geisler D., 2008, ApJ, 682, 135

Lintott C. J., Schawinski K., Slosar A., Land K., Bamford S., Thomas D., Raddick M. J., Nichol R. C., Szalay A., Andreescu D., Murray P., Vandenberg J., 2008, MNRAS, 389, 1179

Liu C., Peng E. W., Jordán A., Ferrarese L., Blakeslee J. P., Côté P., Mei S., 2011, ApJ, 728, 116

López-Sanjuan C., Balcells M., Pérez-González P. G., Barro G., García-Dabó C. E., Gallego J., Zamorano J., 2010, ApJ, 710, 1170

Luo B., Fabbiano G., Strader J., Kim D.-W., Brodie J. P., Fragos T., Gallagher J. S., King A., Zezas A., 2013, ApJS, 204, 14

Masters K. L., Jordán A., Côté P., Ferrarese L., Blakeslee J. P., Infante L., Peng E. W., Mei S., West M. J., 2010, ApJ, 715, 1419

McNeil-Moylan E. K., Freeman K. C., Arnaboldi M., Gerhard O. E., 2012, A&A, 539, A11

Mei S., Blakeslee J. P., Côté P., Tonry J. L., West M. J., Ferrarese L., Jordán A., Peng E. W., Anthony A., Merritt D., 2007, ApJ, 655, 144

Merritt D., 2006, ApJ, 648, 976

Mineo S., Fabbiano G., D'Abrusco R., Fragos T., Kim D.-W., Strader J., Brodie J. P., Gallagher J. S., Zezas A., Luo B., 2014, ApJ, 780, 132

Mink D. J., Wyatt W. F., Caldwell N., Conroy M. A., Furesz G., Tokarz S. P., 2007, in Shaw R. A., Hill F., Bell D. J., eds, Astronomical Data Analysis Software and Systems XVI Vol. 376 of Astronomical Society of the Pacific Conference Series, Automating Reduction of Multifiber Spectra from the MMT Hectospec and Hectochelle. p. 249

Miyazaki S., Komiyama Y., Sekiguchi M., Okamura S., Doi M., Furusawa H., Hamabe M., Imi K., Kimura M., Nakata F., Okada N., Ouchi M., Shimasaku K., Yagi M., Yasuda N., 2002, PASJ, 54, 833

Moore B., Katz N., Lake G., Dressler A., Oemler A., 1996, Nature, 379, 613

Naab T., Oser L., Emsellem E., Cappellari M., Krajnović D., McDermid R. M., Alatalo K., Bayet E., Blitz L., Bois M., Bournaud 2014, MNRAS, 444, 3357

Napolitano N. R., Romanowsky A. J., Coccato L., Capaccioli M., Douglas N. G., Noordermeer E., Gerhard O., Arnaboldi M., de Lorenzi F., Kuijken K., Merrifield M. R., O'Sullivan E., Cortesi A., Das P., Freeman K. C., 2009, MNRAS, 393, 329

Newman J. A., Cooper M. C., Davis M., Faber S. M., Coil A. L., Guhathakurta P., Koo D. C., Phillips A. C., Conroy C., Dutton A. A., Finkbeiner 2013, ApJS, 208, 5

Norris M. A., Gebhardt K., Sharples R. M., Faifer F. R., Bridges T., Forbes D. A., Forte J. C., Zepf S. E., Beasley M. A., Hanes D. A., Proctor R., Kannappan S. J., 2012, MNRAS, 421, 1485

Norris M. A., Kannappan S. J., Forbes D. A., Romanowsky A. J., Brodie J. P., Faifer F. R., Huxor A., Maraston C., Moffett A. J., Penny 2014, MNRAS, 443, 1151

Oser L., Ostriker J. P., Naab T., Johansson P. H., Burkert A., 2010, ApJ, 725, 2312

Ostrov P., Geisler D., Forte J. C., 1993, AJ, 105, 1762

O'Sullivan E., Ponman T. J., Collins R. S., 2003, MNRAS, 340, 1375

Ouchi M., Shimasaku K., Okamura S., Furusawa H., Kashikawa N., Ota K., Doi M., Hamabe M., Kimura M., Komiyama Y., Miyazaki M., Miyazaki S., Nakata F., Sekiguchi M., Yagi M., Yasuda N., 2004, ApJ, 611, 660

Paggi A., Fabbiano G., Kim D.-W., Pellegrini S., Civano F., Strader J., Luo B., 2014, ApJ, 787, 134

Pastorello N., Forbes D. A., Foster C., Brodie J. P., Usher C., Romanowsky A. J., Strader J., Arnold J. A., 2014, MNRAS, 442, 1003

Peng E. W., Jordán A., Côté P., Blakeslee J. P., Ferrarese L., Mei S., West M. J., Merritt D., Milosavljević M., Tonry J. L., 2006, ApJ, 639, 95

Peng E. W., Jordán A., Côté P., Takamiya M., West M. J., Blakeslee J. P., Chen C.-W., Ferrarese L., Mei S., Tonry J. L., West A. A., 2008, ApJ, 681, 197

Pierce M., Beasley M. A., Forbes D. A., Bridges T., Gebhardt K.,

Faifer F. R., Forte J. C., Zepf S. E., Sharples R., Hanes D. A., Proctor R., 2006, MNRAS, 366, 1253

Pierce M., Bridges T., Forbes D. A., Proctor R., Beasley M. A., Gebhardt K., Faifer F. R., Forte J. C., Zepf S. E., Sharples R., Hanes D. A., 2006, MNRAS, 368, 325

Pipino A., D'Ercole A., Chiappini C., Matteucci F., 2010, MNRAS, 407, 1347

Pota V., Forbes D. A., Romanowsky A. J., Brodie J. P., Spitler L. R., Strader J., Foster C., Arnold J. A., Benson A., Blom C., Hargis J. R., Rhode K. L., Usher C., 2013, MNRAS, 428, 389

Proctor R. N., Forbes D. A., Romanowsky A. J., Brodie J. P., Strader J., Spolaor M., Mendel J. T., Spitler L., 2009, MNRAS, 398, 91

Puzia T. H., Kissler-Patig M., Thomas D., Maraston C., Saglia R. P., Bender R., Goudfrooij P., Hempel M., 2005, A&A, 439, 997

Puzia T. H., Kissler-Patig M., Thomas D., Maraston C., Saglia R. P., Bender R., Richtler T., Goudfrooij P., Hempel M., 2004, A&A, 415, 123

Querejeta M., Eliche-Moral M. C., Tapia T., Borlaff A., Rodríguez-Pérez C., Zamorano J., Gallego J., 2014, ArXiv e-prints

Rhode K. L., Zepf S. E., 2001, AJ, 121, 210

Richtler T., Hilker M., Kumar B., Bassino L. P., Gómez M., Dirsch B., 2014, A&A, 569, A41

Romanowsky A. J., Strader J., Brodie J. P., Mihos J. C., Spitler L. R., Forbes D. A., Foster C., Arnold J. A., 2012, ApJ, 748, 29

Rubin V. C., Waterman A. H., Kenney J. D. P., 1999, AJ, 118, 236

Sabatini S., Davies J., van Driel W., Baes M., Roberts S., Smith R., Linder S., O'Neil K., 2005, MNRAS, 357, 819

Sánchez-Blázquez P., Peletier R. F., Jiménez-Vicente J., Cardiel N., Cenarro A. J., Falcón-Barroso J., Gorgas J., Selam S., Vazdekis A., 2006, MNRAS, 371, 703

Sandage A., Bedke J., 1994, The Carnegie Atlas of Galaxies. Volumes I, II.

Sandage A., Tammann G. A., 1981, in Carnegie Inst. of Washington, Publ. 635; Vol. 0; Page 0 Revised Shapley-Ames Catalog of Bright Galaxies. p. 0

Sarazin C. L., Irwin J. A., Bregman J. N., 2001, ApJ, 556, 533

Schauer A. T. P., Remus R.-S., Burkert A., Johansson P. H., 2014, ApJ, 783, L32

Schlafly E. F., Finkbeiner D. P., 2011, ApJ, 737, 103

Schuberth Y., Richtler T., Hilker M., Dirsch B., Bassino L. P., Romanowsky A. J., Infante L., 2010a, A&A, 513, A52

Schuberth Y., Richtler T., Hilker M., Dirsch B., Bassino L. P., Romanowsky A. J., Infante L., 2010b, A&A, 513, A52

Schuberth Y., Richtler T., Hilker M., Salinas R., Dirsch B., Larsen S. S., 2012, A&A, 544, A115

Searle L., Zinn R., 1978, ApJ, 225, 357

Sérsic J. L., 1963, Boletin de la Asociacion Argentina de Astronomia La Plata Argentina, 6, 41

Seth A. C., van den Bosch R., Mieske S., Baumgardt H., Brok M. D., Strader J., Neumayer N., Chilingarian I., Hilker M., McDermid R., Spitler L., Brodie J., Frank M. J., Walsh J. L., 2014, Nature, 513, 398

Shapiro K. L., Genzel R., Förster Schreiber N. M., 2010, MNRAS, 403, L36

Shen J., Gebhardt K., 2010, ApJ, 711, 484

Spitler L. R., Larsen S. S., Strader J., Brodie J. P., Forbes D. A., Beasley M. A., 2006, AJ, 132, 1593

Strader J., Brodie J. P., Cenarro A. J., Beasley M. A., Forbes D. A., 2005, AJ, 130, 1315

Strader J., Fabbiano G., Luo B., Kim D.-W., Brodie J. P., Fragos T., Gallagher J. S., Kalogera V., King A., Zezas A., 2012, ApJ, 760, 87

Strader J., Romanowsky A. J., Brodie J. P., Spitler L. R., Beasley M. A., Arnold J. A., Tamura N., Sharples R. M., Arimoto N., 2011, ApJS, 197, 33

Strader J., Seth A. C., Forbes D. A., Fabbiano G., Romanowsky A. J., Brodie J. P., Conroy C., Caldwell N., Pota V., Usher C., Arnold J. A., 2013, ApJ, 775, L6

Tal T., van Dokkum P. G., 2011, ApJ, 731, 89

Tal T., van Dokkum P. G., Nelan J., Bezanson R., 2009, AJ, 138, 1417

Tasca L. A. M., Le Fèvre O., López-Sanjuan C., Wang P.-W., Cassata P., Garilli B., Ilbert O., Le Brun V., Lemaux B. C., Maccagni D., Tresse 2014, A&A, 565, A10

Teodorescu A. M., Méndez R. H., Bernardi F., Thomas J., Das P., Gerhard O., 2011, ApJ, 736, 65

Tonini C., 2013, ApJ, 762, 39

Usher C., Forbes D. A., Brodie J. P., Foster C., Spitler L. R., Arnold J. A., Romanowsky A. J., Strader J., Pota V., 2012, MN-RAS, 426, 1475

van de Ven G., van den Bosch R. C. E., Verolme E. K., de Zeeuw P. T., 2006, A&A, 445, 513

van Dokkum P. G., Bezanson R., van der Wel A., Nelson E. J., Momcheva I., Skelton R. E., Whitaker K. E., Brammer 2014, ApJ, 791, 45

Vanderbeke J., West M. J., De Propris R., Peng E. W., Blakeslee J. P., Jordán A., Côté P., Gregg M., Ferrarese L., Takamiya M., Baes M., 2014, MNRAS, 437, 1725

vanDokkum P. G., 2001, PASP, 113, 1420

Veljanoski J., Mackey A. D., Ferguson A. M. N., Huxor A. P., Côté P., Irwin M. J., Tanvir N. R., Peñarrubia J., Bernard E. J., Fardal M., Martin N. F., McConnachie A., Lewis G. F., Chapman S. C., Ibata R. A., Babul A., 2014, MNRAS, 442, 2929

Vika M., Driver S. P., Cameron E., Kelvin L., Robotham A., 2012, MNRAS, 419, 2264

Vitvitska M., Klypin A. A., Kravtsov A. V., Wechsler R. H., Primack J. R., Bullock J. S., 2002, ApJ, 581, 799

White S. D. M., Rees M. J., 1978, MNRAS, 183, 341

Woodley K. A., Gómez M., Harris W. E., Geisler D., Harris G. L. H., 2010, AJ, 139, 1871

Woodley K. A., Harris W. E., 2011, AJ, 141, 27

Wu X., Gerhard O., Naab T., Oser L., Martinez-Valpuesta I., Hilz M., Churazov E., Lyskova N., 2014, MNRAS, 438, 2701

Young L. M., Rosolowsky E., van Gorkom J. H., Lamb S. A., 2006, ApJ, 650, 166

Zhang H.-X., Peng E. W., Cote P., Liu C., Ferrarese L., Cuillandre J.-C., Caldwell 2015, ArXiv e-prints

Zolotov A., Willman B., Brooks A. M., Governato F., Brook C. B., Hogg D. W., Quinn T., Stinson G., 2009, ApJ, 702, 1058